Research Square

Preprints are preliminary reports that have not undergone peer review.
They should not be considered conclusive, used to inform clinical practice,
or referenced by the media as validated information.

Mitochondrial Dysfunction fuels Osimertinib Resistance via the Pyruvate-Acetaldehyde-Acetate (PAA) Metabolic Bypass in EGFR-Mutant NSCLC

Elena Levantini

elena.levantini@itb.cnr.it

Institute for Biomedical Technologies: Istituto di Tecnologie Biomediche Consiglio Nazionale delle Ricerche https://orcid.org/0000-0003-4612-3105

Research Article

Keywords: Non-Small Cell Lung Cancer, osimertinib, EGFR-mutant NSCLC, EGFR-TKI resistance, transcriptomics, genomics, metabolomics, exometabolome, mitochondria, mitochondrial mechanisms, ATP synthase, PAA pathway

Posted Date: August 12th, 2026

DOI: https://doi.org/10.21203/rs.3.rs-10663868/v1

License: This work is licensed under a Creative Commons Attribution 4.0 International License.
Read Full License

Additional Declarations: The authors declare no competing interests.

Mitochondrial Dysfunction fuels Osimertinib Resistance via the Pyruvate-Acetaldehyde-Acetate (PAA) Metabolic Bypass in EGFR-Mutant NSCLC

Giorgia Maroni[1], Eva Cabrera San Millan[1], Raffaella Mercatelli[1], Alessandra Gatta[2], Maddalena Di Nardo[1], Fabrizia Carli[3], Maria Magallon-Mosella[4,5], Michele Menicagli[6], Alice Chiodi[7], Ludovica Celli[7], Roberta Alfieri[7], Naomi Scarano[7], Beatrice Campanella[2], Massimo Onor[2], Letizia Modeo[8], Paride Pelucchi[7], Giulia Braccini[1], Giovanni Cercignani[9], Damia Romero-Moya[4,5], Ivan Merelli[7], Alessandro Orro[7], Pasqualina D'Ursi[7], Azhar Ali[10], Ettore Mosca[7], Amalia Gastaldelli[3], Alessandra Giorgetti[4,5,11], Emilia Bramanti[2*^], Elena Levantini[1,6*^]

[1]*CNR-Consiglio Nazionale delle Ricerche, Istituto di Tecnologie Biomediche (ITB-CNR), SS di Pisa, Area della Ricerca di Pisa, Italy*
[2]*CNR-Consiglio Nazionale delle Ricerche, Istituto di Chimica dei Composti OrganoMetallici (ICCOM-CNR), SS di Pisa, Area della Ricerca di Pisa, Italy*
[3]*CNR-Consiglio Nazionale delle Ricerche, Istituto di Fisiologia Clinica (IFC-CNR), Pisa, Area della Ricerca di Pisa, Italy*
[4]*Hematopoietic Stem Cell Biology and Leukemogenesis, Regenerative Medicine Program, Bellvitge Institute for Biomedical Research (IDIBELL), L'Hospitalet de Llobregat, Spain.*
[5]*Program for Advancing the Clinical Translation of Regenerative Medicine of Catalonia, P-CMR[C], Barcelona, Spain.*
[6]*Fondazione Pisana per la Scienza ONLUS (FPS), San Giuliano Terme, Pisa, Italy*
[7]*CNR-Consiglio Nazionale delle Ricerche, Istituto di Tecnologie Biomediche (ITB-CNR), Segrate (Milan), Italy*
[8]*Dipartimento di Biologia, Università di Pisa, Pisa, Italy;*
[9]*Scuola Normale di Pisa, Class of Sciences, Pisa, Italy;*
[10]*Cancer Science Institute of Singapore, National University of Singapore, Singapore*
[11]*Department of Pathology and Experimental Therapeutics, Faculty of Medicine and Health Sciences, Barcelona University, Barcelona, Spain.*

***^: co-last, co-corresponding**

Correspondence to: elena.levantini@itb.cnr.it; emilia.bramanti@pi.iccom.cnr.it

Conflict of Interest: The authors declare that they have no conflict of interest.

Running title: Drug resistance mechanisms

ABSTRACT

Osimertinib (Osi) resistance remains a major challenge in EGFR-mutant NSCLC. To uncover the underlying mechanisms, we performed integrated transcriptomic, metabolomic, genomic, structural (including advanced 3D imaging of mitochondrial networks), and functional analyses in matched H1975 parental (Par) and Osi-resistant (OsiR) cells.

OsiR cells display mitochondrial dysfunction characterized by impaired oxidative phosphorylation (OXPHOS), altered mitochondrial gene expression, and accumulation of mutations in both mitochondrial DNA and nuclear-encoded mitochondrial genes. A K45Q mutation in MT-ATP8 may contribute to mitochondrial remodeling associated with this resistant phenotype. Genetic ablation of *Aldh2* significantly restores osimertinib sensitivity, identifying aldehyde dehydrogenase-dependent metabolism as a functional contributor to resistance.

We introduce *mitochondriomics* to describe this multilayered remodeling, integrating genomic, transcriptomic, structural, and functional changes. Metabolomic profiling revealed extracellular accumulation of pyruvate, lactate, acetaldehyde, and acetate**,** reflecting enhanced glycolysis and activation of an alternative pyruvate-acetaldehyde-acetate (PAA) adaptive pathway. Stable-isotope tracing revealed increased extracellular accumulation of glucose-derived acetate in resistant cells. Together with ALDH2 loss-of-function studies, these findings support a role for PAA-associated metabolism in maintaining metabolic homeostasis during drug resistance, while the non-oxidative pentose phosphate pathway (non-oxPPP) contributes to biosynthetic demands.

Single-cell analyses of genetically paired transgenic mice revealed that resistant tumors are enriched in pulmonary epithelial AT2-like subpopulations, which recapitulate the mitochondrial remodeling and bioenergetic signatures observed *in vitro*.

These findings uncover a mitochondria-centered adaptive program in Osi-resistant EGFR-mutant NSCLC, where mitochondrial remodeling and the PAA-associated metabolic adaptation converge to promote survival and drug tolerance. The work highlights metabolic vulnerabilities with potential therapeutic relevance to overcome osimertinib resistance.

Keywords: Non-Small Cell Lung Cancer, osimertinib, EGFR-mutant NSCLC, EGFR-TKI resistance, transcriptomics, genomics, metabolomics, exometabolome, mitochondria, mitochondrial mechanisms, ATP synthase, PAA pathway.

[SIGNIFICANCE]

Osimertinib resistance in EGFR-mutant NSCLC is driven by metabolic rewiring. Using integrated omics, functional assays, structural analyses, and 3D imaging, we identify a novel pyruvate-acetaldehyde-acetate (PAA) adaptive pathway that contributes to metabolic adaptation and resistance maintenance under drug pressure. A K45Q mutation in MT-ATP8 may contribute to mitochondrial remodeling associated with this metabolic adaptation. Genetic ablation of *Aldh2* restores osimertinib sensitivity, identifying ALDH-associated metabolism as a functional contributor to resistance.

Through these analyses, mitochondria emerge as both sensors and effectors of adaptive metabolism, revealing actionable vulnerabilities and offering a mitochondria-centered strategy to enhance osimertinib efficacy.

INTRODUCTION

Resistance to tyrosine kinase inhibitors (TKIs) such as osimertinib represents a significant clinical challenge in the treatment of EGFR-mutant NSCLC. The mechanisms driving osimertinib resistance are complex and multifactorial, involving both EGFR-dependent and -independent pathways [1]. These include secondary mutations, activation of alternative signaling cascades, alterations in downstream effectors, and phenotypic adaptations within both cancer cells and the tumor microenvironment (TME).

Our previous work identified two metabolic alterations associated with TKI-resistant EGFR-mutated NSCLC. First, we found that the palmitoylation of EGFR, regulated by Fatty Acid Synthase (FASN), influences EGFR stability and can be inhibited by Orlistat, partially mitigating resistance [2]. Second, we showed that the interaction between Caveolin-1 and the glucose transporter GLUT3 enhances glucose uptake, a process that can be disrupted by Atorvastatin, impacting resistance mechanisms [3]. These findings motivated our investigation into metabolic vulnerabilities exploitable to overcome TKI resistance.

Abnormal cellular metabolism supports tumor progression and therapeutic resistance, yet the mechanisms of metabolic rewiring in TKI-resistant NSCLC remain elusive. Cancer cells, including NSCLC, redistribute bioenergetic reliance, selectively remodeling mitochondrial OXPHOS, while increasing glycolytic activity, a phenomenon known as the Warburg effect, supporting survival and drug resistance [4-6]. Yet, the role of mitochondria in TKI resistance remains underexplored.

Acetate metabolism is another underappreciated contributor. Since the 1950s, it has been known that tumor cells preferentially utilize pyruvate or acetate for biosynthetic needs [7, 8]. Under hypoxia, cancer cells often rely on acetate to generate acetyl-CoA, underscoring the importance of mitochondrial function in sustaining tumor growth and therapeutic resistance [9, 10]. Balancing intracellular acetyl-CoA and acetate is critical under nutrient-limiting conditions. How acetate metabolism, glycolysis, OXPHOS, and mitochondrial dynamics interconnect in TKI resistance remains unclear. We aimed to fill this gap by investigating acetate metabolism and mitochondrial reprogramming in osimertinib resistance in EGFR-mutant NSCLC.

Using the H1975 NSCLC cell line (*EGFR L858R/T790M*), carrying a common resistance genotype, we applied an integrated multi-omics and functional approach to identify key metabolic biomarkers of osimertinib resistance. To capture the full extent of these alterations, we introduce *mitochondriomics*: a multidimensional characterization of mitochondrial structures, function, and regulation, encompassing mitochondrial genomics, transcriptomics, structural dynamics, and metabolic output.

A central focus was the analysis of the extracellular medium (ECM) via exometabolome profiling using chromatography-based assays [11-14] to identify metabolites supporting cancer cell survival. This revealed defined metabolic signatures, including elevated extracellular acetate and other metabolites in resistant cells. Mitochondrial dynamics were altered, together with evidence of non-oxidative pentose phosphate pathway (non-oxPPP) remodeling.

Notably, the pyruvate-acetaldehyde-acetate (PAA) pathway emerged as a prominent feature of resistant cells, characterized by extracellular accumulation of pyruvate, acetaldehyde, and acetate, activation of aldehyde metabolism, and remodeling of pathways involved in metabolic homeostasis.

Stable-isotope tracing demonstrated increased glucose-derived acetate production and extracellular accumulation in resistant cells. This metabolic rewiring was reinforced by a disruptive K45Q mutation in the mitochondrial ATP synthase subunit MT-ATP8 that may contribute to mitochondrial remodeling associated with the resistant phenotype, further linking mitochondrial adaptation to the metabolic changes observed in resistant cells. Genetic ablation of *Aldh2* restored osimertinib sensitivity, identifying ALDH-associated metabolism as a functional contributor to resistance. Overall, our studies identify the PAA pathway as a key component of the metabolic adaptation associated with osimertinib resistance in EGFR-mutant NSCLC.

2. RESULTS

2.1 RNA sequencing reveals the glycolytic adaptation of osimertinib-resistant EGFR mutant NSCLC cells

To uncover transcriptional changes associated with osimertinib resistance, we performed RNA sequencing of Par and OsiR H1975 cells, a resistant model recently developed and characterized by our group [15]. Differential gene expression (DGE) analysis identified broadly dysregulated genes, with LogFC ≥ 0.25 and FDR ≤ 0.05 as thresholds.

Pathway enrichment analyses consistently pointed to mitochondrial remodeling as a central feature of resistance. EnrichR revealed significant involvement of mitochondrial processes in OsiR cells, including *Mitochondrial Translation*, *Mitochondrial Gene Expression*, and *Cellular Response to Oxidative Stress* in the Gene Ontology (GO) Biological Process (BP) category (adjusted p-value <0.05) (**Figure 1a**). GO Cell Compartment (CC) analysis further highlighted *Mitochondrial Ribosomes*, *Mitochondrial Membrane*, and *Mitochondrial Inner Membrane*, underscoring mitochondria as central to the adaptive program.

HallMark (HM) pathway analysis confirmed enrichment in *Hypoxia* and *Reactive Oxygen Species (ROS) Pathway*, reinforcing the importance of redox regulation in the resistant phenotype. HM also highlighted *Glycolysis* and *Oxidative Phosphorylation*, suggesting a dynamic energy shift. *Glycolysis* enrichment reflects a canonical adaptive strategy of cancer cells under therapeutic pressure, enabling OsiR cells to survive chronic drug exposure. Complementary WikiPathways (WP) analysis confirmed involvement of *Oxidative Stress Response* and *Mitochondrial Complex IV Assembly*, linking mitochondrial homeostasis to acquired drug resistance.

Across GO-BP, HM and WP analyses, genes driving ROS generation were significantly upregulated, indicative of heightened oxidative stress, likely resulting from mitochondrial dysfunction and increased metabolic activity. Transcriptomic data also revealed upregulation of glutathione metabolism genes, including *glutathione synthetase (GSS)* and *glutathione S-transferase Mu 3 (GSTM3)*, as well as ROS-scavenging genes like *superoxide dismutase 1 (SOD1)* and *superoxide dismutase 2 (SOD2)* (**Figure 1b**), suggesting OsiR cells enhance detoxification capacity to survive oxidative stress.

In addition, metabolic enzymes associated with cancer progression [16-19] were upregulated, including *Lactate Dehydrogenase C (LDHC)*, *Aldehyde Dehydrogenase 2 (ALDH2)* and *Aldehyde Dehydrogenase 7 Family Member A1 (ALDH7A1)* (**Figure 1b**), with Western blot confirming increased ALDH2 and ALDH7A1 protein levels (**Figure 1c**). These enzymes contribute to aldehyde detoxification and metabolic resilience, supporting a model of stress-adaptive metabolic rewiring in OsiR cells.

Importantly, this rewiring includes a strategic realignment of mitochondrial function, reflecting a coordinated adaptation, which we term a *mitochondriomic shift*, that maintains redox balance and sustains survival under therapeutic pressure.

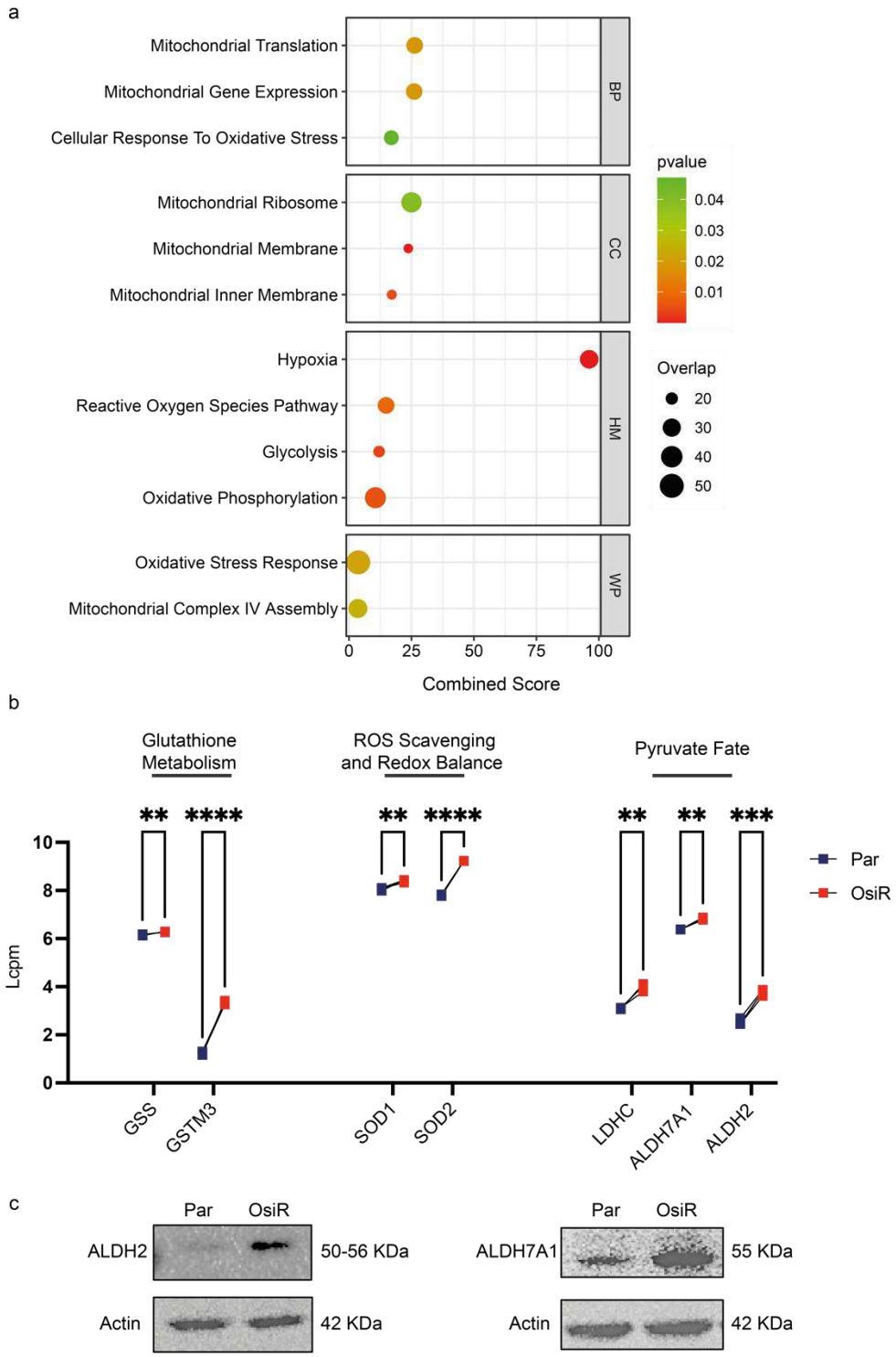

Figure 1. Transcriptomic analysis highlights metabolic adaptation in osimertinib-resistant EGFR mutant NSCLC cells. **(a)** Pathway enrichment analysis of differentially expressed genes in OsiR versus Par H1975 cells using EnrichR. Upregulated pathways are shown across Gene Ontology (GO) categories, Biological Processes (BP) and Cellular Components (CC), as well as Hallmark (HM) and WikiPathways (WP). Dot size indicates gene overlap; color represents adjusted p-value. **(b)** RNAseq analysis showing increased expression of genes involved in glutathione metabolism, ROS scavenging and redox balance, as well as pyruvate metabolism in H1975 Par (blue) and OsiR (red) cells. Statistical significance is indicated. Data are shown as mean ± SD; n=3 Par, n=3 OsiR. Welch's t-test. 0.0332 (*), 0.0021 (**), 0.0002 (***), <0.0001 (****). **(c)** Western blot analyses of H1975 Par and OsiR cells. Protein lysates were immunoblotted with antibodies against ALDH2 and ALDH7A1. β-actin was used as a loading control. Expected molecular weights (kDa) are indicated.

2.2 Distinct Mitochondrial Morphological Alterations in osimertinib-resistant EGFR mutant NSCLC cells

To investigate the link between metabolic remodeling and mitochondrial architecture, we employed 3D confocal reconstruction of mitochondrial networks in Par and OsiR cells. OsiR cells exhibited a fragmented, toroidal mitochondrial morphology with reduced size, consistent with network disruption, whereas Par cells displayed

elongated and interconnected mitochondria, indicative of a fused and functional network (**Figure 2a**). These differences support mitochondrial fragmentation associated with stress adaptation and therapy resistance, consistent with reduced reliance on OXPHOS and increased metabolic flexibility [20-22].

Quantitative 3D analysis confirmed these observations. Compared with Par cells, OsiR cells showed reduced mitochondrial volume, surface area, total branch number, branch length, junctions, and endpoints per mitochondrion, alongside increased sphericity and higher mitochondrial number per cell (**Figure 2b**), indicating a shift toward a fragmented, stress-responsive phenotype under osimertinib pressure.

Western blot analysis further revealed an imbalance in mitochondrial dynamics regulators. OsiR cells exhibited increased Dynamin-Related Protein 1 (DRP1), a key driver of mitochondrial fission (**Figure 2c**), while Mitofusin 2 (MFN2), a central regulator of fusion, was more abundant in Par cells (**Figure 2c**), demonstrating a shift toward mitochondrial fragmentation consistent with altered mitochondrial dynamics in resistant cells. Additionally, OsiR cells displayed elevated Voltage-Dependent Anion Channel (VDAC) expression (**Figure 2c**), supporting altered outer mitochondrial membrane integrity and mitochondrial remodeling under sustained drug-induced stress [23-25].
Collectively, these morphological and molecular alterations indicate major reprogramming of mitochondrial architecture in OsiR cells, providing a structural framework for metabolic and genomic adaptation during resistance acquisition.

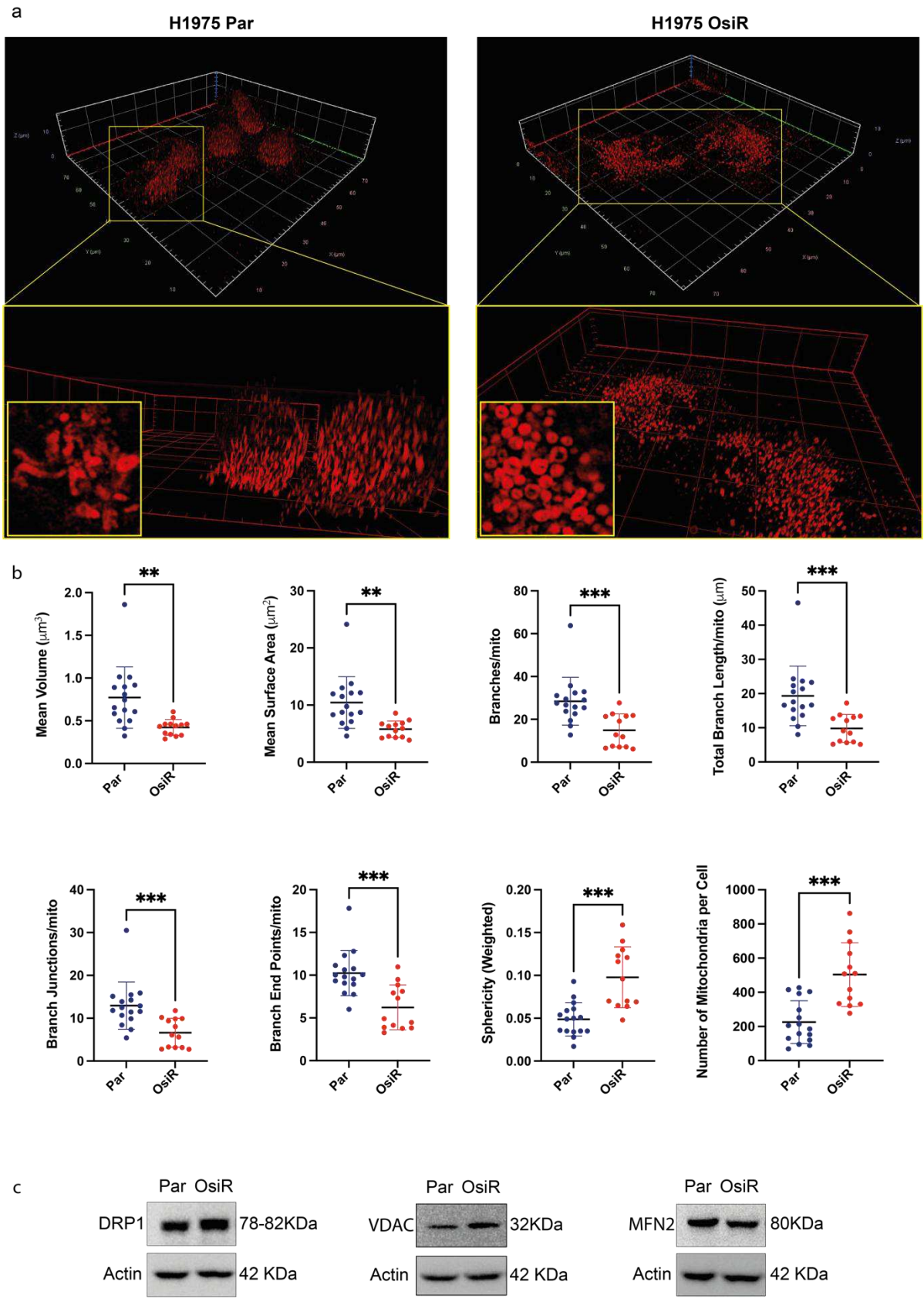

Figure 2. Mitochondrial imaging and protein analysis highlight mitochondrial structural remodeling in osimertinib-resistant EGFR mutant NSCLC cells.

(a) Leica Airyscan confocal microscopy 3D reconstruction of mitochondria in H1975 cells. MITO-ID staining (red channel) of mitochondria in Par H1975 cells (left panel) and in OsiR H1975 cells (right panel). Insets show zoomed-in views of mitochondrial architecture. **(b)** Quantitative 3D morphometric analysis of mitochondria performed using the Mitochondria Analyzer plugin in Fiji. Error bars represent standard deviation (SD); p-values are indicated (n=16 Par, n=13 OsiR; Welch's t-test; 0.0332 (*), 0.0021 (**), 0.0002 (***), <0.0001 (****). **(c)** Western blot analyses of H1975 Par and OsiR cells. Protein lysates were immunoblotted with antibodies against DRP1, MFN2 and VDAC. β-actin was used as a loading control. Expected molecular weight (kDa) is indicated.

2.3 Mitochondrial and Nuclear Genome mutations as Bioenergetic Adaptations in Osimertinib Resistance

To investigate genomic alterations associated with osimertinib resistance, we performed targeted mitochondrial DNA sequencing (mtDNA-seq) and whole-genome sequencing (WGS) of nuclear DNA in Par and OsiR cells. This integrated analysis revealed selective alterations of OXPHOS genes consistent with adaptive mitochondrial remodeling under sustained drug pressure, rather than stochastic mutational accumulation, in line with the fragmented, stress-responsive mitochondrial phenotype of OsiR cells.

Mitochondrial Genome Remodeling

Mitochondrial sequencing identified 171 mtDNA variants and extensive turnover during resistance acquisition, characterized by selective loss of pre-existing parental variants, emergence of OsiR-specific mutations, and enrichment of a subset of pre-existing variants **(Suppl. Table 1, Suppl. Data 1)**. Remodeling was particularly pronounced across electron transport chain (ETC) complexes.

Complexes I, IV, and V displayed extensive loss of parental variants (80-94%) with selective acquisition of resistance-specific mutations, consistent with functional rewiring under drug pressure. Complex III showed a predominance of OsiR-specific MT-CYB variants **(Figure 3a)**, suggesting that mitochondrial genomic remodeling may contribute to ETC destabilization. Complex IV exhibited widespread loss of Par-specific variants across MT-CO1, MT-CO2, and MT-CO3, with only a small fraction retained at reduced allele frequency (AF) and limited emergence of OsiR-specific variants (**Figure 3a, Suppl. Table 1 and Suppl. Data 1**). Transcriptomic enrichment of *Mitochondrial Complex IV Assembly* pathways **(Figure 1a**), suggested compensatory transcriptional reinforcement of C-IV biogenesis and structural optimization. Although no novel coding mutations emerged in Complex IV genes, COXIV protein levels were reduced **(Figure 3d)**, without changes in mRNA expression (data not shown), indicating post-transcriptional regulation.

Nuclear Genome Remodeling

WGS of nuclear-encoded OXPHOS genes revealed parallel adaptive changes, with 71.9% of variants showing reduced AF in OsiR cells. Complex I showed heterogeneous, subunit-specific gains and losses **(Figure 3b)**, with selected variants (e.g., NDUFAF6, NDUFB1, NDUFA7 and NDUFS2) enriched by up to 15.5-fold in AF, while others were negatively selected, indicating selective pressure on discrete functional modules. In contrast, Complex II remained largely stable (**Suppl. Table 1 and Suppl. Data 2**), with only one enriched *SDHA* variant (7.63-fold) in OsiR cells **(Figure 3b)**, despite increased SDH expression **(Figure 3c)**, suggesting non-genetic adaptation. Complex III showed decreased nuclear-encoded subunit variants **(Figure 3b)**, consistent with ETC destabilization and impaired electron transfer. This pattern was further supported by reduced *MT-CYB* transcript levels ($\log_2$FC -0.7; adjusted p-value = 7.33×10^{-6}), which represents the only mtDNA-encoded subunit of this complex [26]; decreased Prohibitin 1 (PHB1) protein, a key scaffold for Complex III assembly **(Figure 3c)**, and reduced nuclear CYCS variant frequency (encoding cytochrome c, the mobile electron shuttle between C-III and C-IV) with lower cytochrome c protein levels (**Figure 3b, 3d; Suppl. Table 1 and Suppl. Data 2**). Complex IV nuclear variants exhibited heterogeneous AF changes across structural subunits and assembly factors **(Figure 3b)**, particularly among subunits regulating supercomplex assembly, suggesting impaired electron transfer at the Complex III-IV interface.

Resistance involved few genes contributing to both catalytic complexes and higher-order ETC organization (**Figure 3b, Suppl. Table 1, Suppl. Data 2**). COX7A2L (Complex IV; stabilizes III/IV supercomplexes) [27] and RAB5IF (respirasome assembly) [28] were enriched in OsiR cells (4.14- and 8.76-fold), while COA1 (Complex I; respirasome) was higher in Par cells (1.87-fold), highlighting selective remodeling of structural components spanning multiple complexes.

Complex V Undergoes Extensive Genomic Remodeling During Resistance Acquisition

ATP synthase, the terminal enzyme of the respiratory chain responsible for coupling the proton motive force to ATP production, emerged as one of the most extensively remodeled OXPHOS complexes during resistance acquisition.

Both mtDNA-encoded subunits, MT-ATP6 and MT-ATP8, exhibited extensive loss of parental variants, with reductions of 80% and 50%, respectively, and the emergence of OsiR-specific mutations (**Figure 3a, Suppl. Table 1, Suppl. Data 1**). Concurrently, nuclear-encoded subunits underwent selective pruning, with 49 out of 52 variants enriched in Par cells and only three variants showing increased AF in OsiR cells (**Figure 3b; Suppl. Data 2**). Among these, a non-synonymous MT-ATP8 mutation (K45Q) emerged as a candidate potentially linking mitochondrial genomic remodeling to functional impairment of ATP synthase **(Figure 3a; Suppl. Table 1, Suppl. Data 1-2).** This coordinated remodeling suggests a selective attenuation of canonical ATP synthesis, likely favoring metabolic flexibility under drug pressure.

Supplementary Table 1. Distribution of mitochondrial (mtDNA-seq) and nuclear (WGS) variants across OXPHOS complexes in Par and OsiR cells. Mutations specific to Par cells or showing higher allele frequency (AF) in Par are indicated in blue, whereas mutations specific to OsiR cells or enriched in OsiR are indicated in red. Grey background indicates variants detected by mtDNA sequencing, while light blue background indicates variants detected by whole-genome sequencing. Genes participating in multiple respiratory complexes or in respirasome/supercomplex assembly are indicated in combined categories. Numbers represent absolute variant counts; corresponding percentages are reported in the main text.

			shared	shared				
	Par- Specific	OsiR-Specific	Par>OsiR	OsiR>Par	TOT	Par>OsiR	OsiR>Par	TOT
Complex I	56	23	11	3	93	14	17	31
Complex I;Complex IV						1		1
Complex II						2	1	3
Complex III		10	1	1	12	6		6
Complex IV	47	2	3		52	14	11	25
Complex IV;Respirasome assembly							1	1
Complex V	10	3		1	14	49	3	52
Cytochrome C						1		1
Respirasome assembly							1	1
Total (by condition)	113	38	15	5	171	87	34	121
Sequencing (mtDNA-seq or WGS)	171				171	121		121

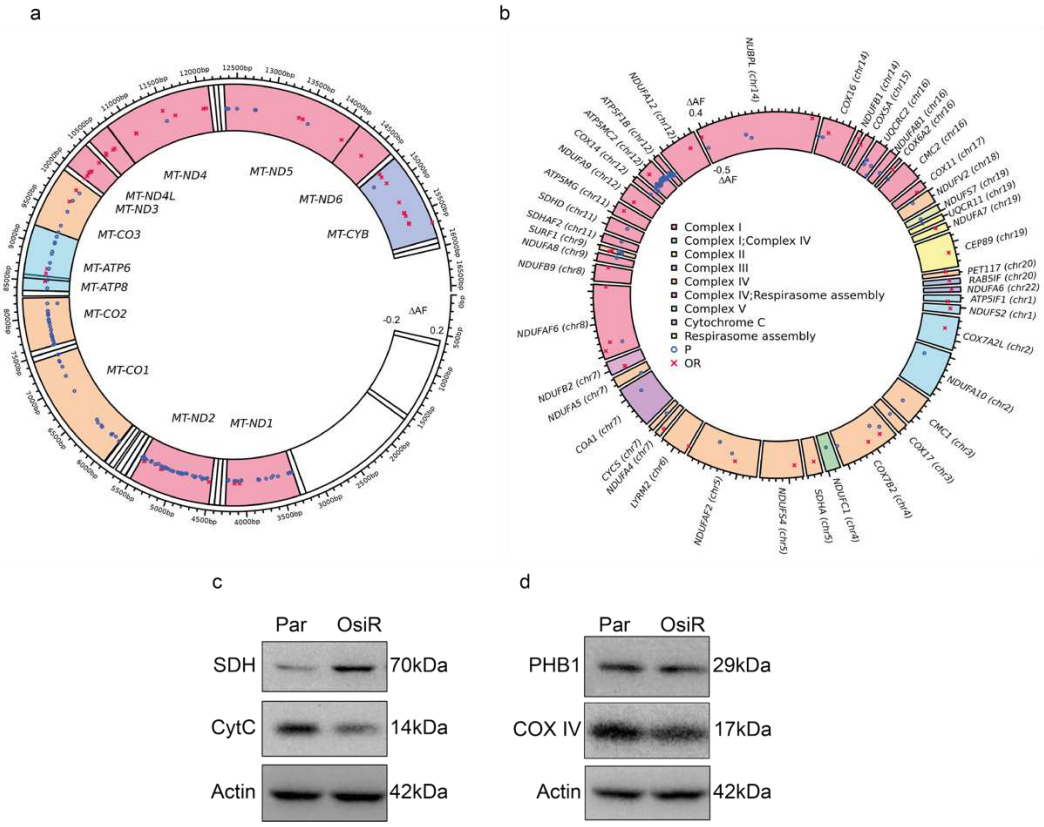

Figure 3. Mitochondrial and nuclear genome remodeling in osimertinib-resistant EGFR mutant NSCLC cells. (a) Mitochondrial and **(b)** nuclear genome mutations in H1975 Par versus OsiR cells, mapped by genomic location (across the circle)

and difference in Allele Frequency (ΔAF, radial axis). Blue circles indicate mutations present in Par cells that were lost in OsiR cells (ΔAF < 0); red crosses represent mutations gained in OsiR cells (ΔAF > 0). Mitochondrial genes are color-coded by respiratory complex. **(c-d)** Western blot analyses of H1975 Par and OsiR cells. Protein lysates were immunoblotted with antibodies against SDH, CytC, PHB1 and COX IV. β-actin was used as a loading control. Expected molecular weights (kDa) are indicated.

2.4 Structural and Predicted Functional Implications of the MT-ATP8 Mutation

Among mtDNA variants detected in OsiR cells, we identified a somatic 8498A>C substitution in *MT-ATP8*, resulting in a lysine-to-glutamine change at position 45 (K45Q) and predicted to be probably damaging (PolyPhen-2 0.939). ATP8 is a membrane-embedded component of the F_0 domain of ATP synthase (Complex V) [29], contributing to structural stabilization and torque transmission to the F_1 catalytic head through the central (γ, δ, ε) and peripheral (F6, b, d) stalks, coupling proton translocation to rotary catalysis (**Figure 4a,b**). Parental cells retained WT ATP8, enabling direct structural comparison.

To evaluate the structural impact of this mutation, we performed 100-ns molecular dynamics (MD) simulations of the human ATP synthase monomer (Cryo-EM structure, PDB ID: 8H9T) [30], embedded in a lipid bilayer, modeling both WT and K45Q complexes. Trajectory clustering revealed distinct conformational states, with the mutant preferentially occupying the dominant state (56.9% versus 41% in WT), indicating mutation-induced rearrangement of the conformational landscape (**Suppl. Fig. S1a,b**).

Principal Component Analysis (PCA) showed that the major mode of structural variability (PC1) was markedly altered in the K45Q mutant, with enhanced flexibility in the central stalk, the ATP8 intramembrane region, and neighboring F_0 subunits (a, e, f, g) (**Suppl. Fig. S2b**). Consistently, Root Mean Square Fluctuation (RMSF) demonstrated increased residue-level flexibility in these regions in K45Q compared with WT, whereas the WT complex exhibited more constrained and coordinated dynamics across the enzyme (**Suppl. Fig. S3**). Together, these analyses suggest that K45Q may remodel ATP synthase dynamics, introducing local flexibility while weakening global mechanical coordination. In WT, coordinated movements of the central and peripheral stalks facilitate efficient torque transmission between the F_0 and F_1 domains (**Suppl. Figs. S2a, S3**). By contrast, K45Q disrupted this coupling, with altered compaction of the peripheral stalk (d, F6), and enhanced flexibility in the central stalk, the ATP8 intramembrane region, and neighboring F_0 subunits, suggesting impaired mechanical communication between membrane and catalytic domains and reduced long-range coordination across the enzyme.

At the molecular level, substitution of Lys45 with a neutral glutamine altered the local electrostatic environment and hydrogen-bonding network surrounding ATP8, reshaping its packing and interaction specificity with neighboring subunits. Several WT contacts were lost, and mutation-specific interactions emerged (**Suppl. Table S2**), consistent with altered subunit packing and reduced Complex stability. Dynamic cross-correlation analyses further revealed rewiring of collective motions within the ATP synthase complex. In the K45Q mutant, intramembrane ATP8 residues exhibited altered correlations with multiple F_0 subunits (6.8PL, f, g) and with the F_1 α/β catalytic chains, accompanied by increased anticorrelation with both the central and peripheral stalks. Extramembrane ATP8 residues displayed higher variability, indicating region-specific hypoflexibility and disruption of long-range dynamic coordination (Suppl. Figs. S4, S5).

Normal Mode Analysis (NMA) identified intrinsic low-frequency vibrational modes associated with functionally relevant collective motions [31-33], provided mechanistic insight into the effects of K45Q (**Figure 5a**). In WT, Mode 11 captured spring-like compression-extension of the peripheral stalk (b subunit, **Figure 5b**), coherent vertical oscillations of F_0 subunits e, f, and g (**Figure 5d**), and coordinated rotation of central stalk subunits (γ, δ, ε) with the c_8-ring relative to the catalytic head (**Figure 5f**), reflecting efficient torque transmission and coherent rotary mechanics. By contrast, K45Q disrupted these collective motions: the peripheral stalk b-subunit oscillated erratically, with back-and-forth displacements (**Figure 5c**), F_0 subunits e, f, and g rotated irregularly rather than vertically (**Figure 5e**), and central stalk subunits γ, δ, ε moved incoherently with the c_8-ring and catalytic head (**Figure 5g**), consistent with impaired mechanical coupling and partial uncoupling of ATP synthesis.

Overall, the K45Q mutation is predicted to destabilize ATP synthase both structurally and dynamically, reshaping inter-subunit interactions and weakening long-range coupling between F_0 and F_1 domains. These perturbations are consistent with a partially uncoupled enzyme state, likely contributing to reduced OXPHOS efficiency while preserving overall Complex integrity. Importantly, the convergence of multiple complementary analyses, including MD, PCA, RMSF, cross-correlation, and NMA, provides consistent mechanistic insight and ensures robust characterization of the mutant phenotype.

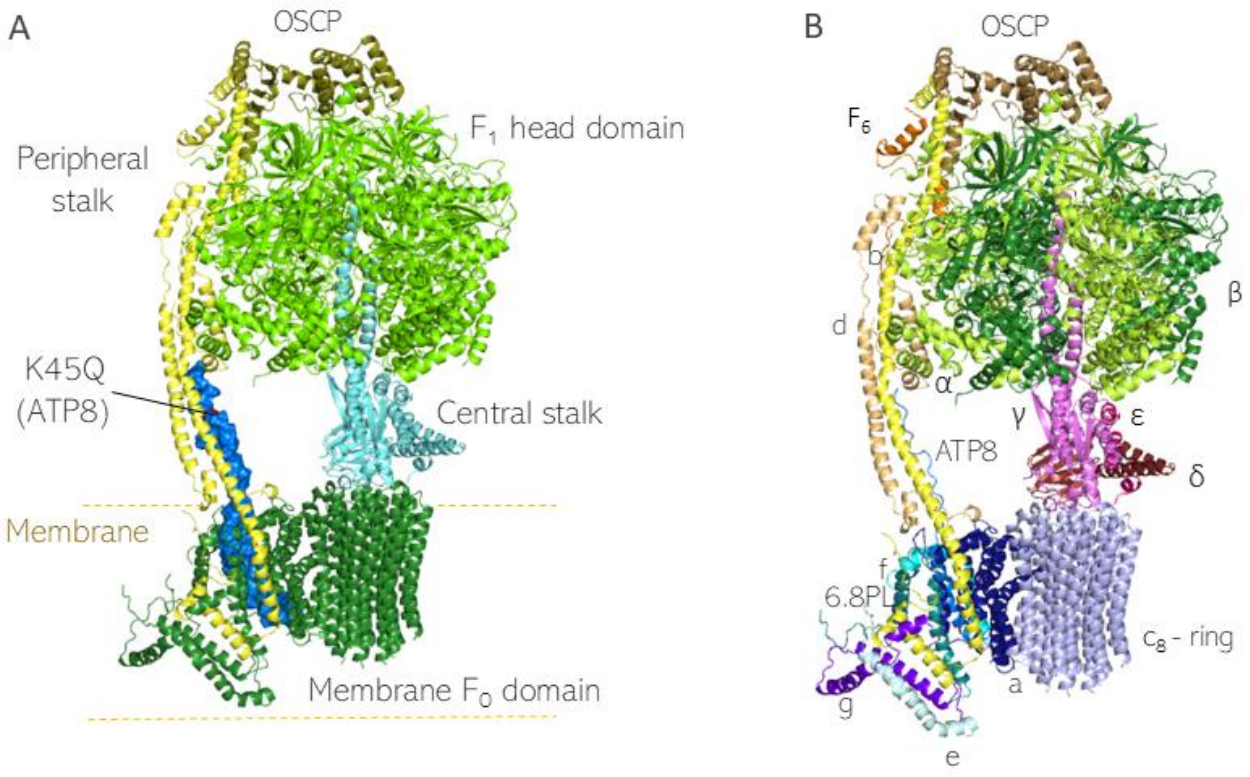

Figure 4. Structural representation of the mitochondrial F_1F_0-ATPase highlighting K45Q-associated structural alterations. **(A)** Representative frame of the F_1F_0-ATPase showing the F_1 catalytic head (light green), peripheral stalk (yellow), F_0 domain (dark green), central stalk (cyan), and OSCP (deep olive). The ATP8 chain is depicted as a blue surface, with the mutated residue K45Q highlighted in red. **(B)** Subunit organization of the complex: α (light green), β (dark green), γ (violet), ε (hot pink), δ (raspberry), b (yellow), d (orange-yellow), F6 (orange), OSCP (brown), c_8-ring (pale blue), a (dark blue), ATP8 (bright blue), f (cyan), g (purple-blue), e (pale cyan), and 6.8PL (deep teal).

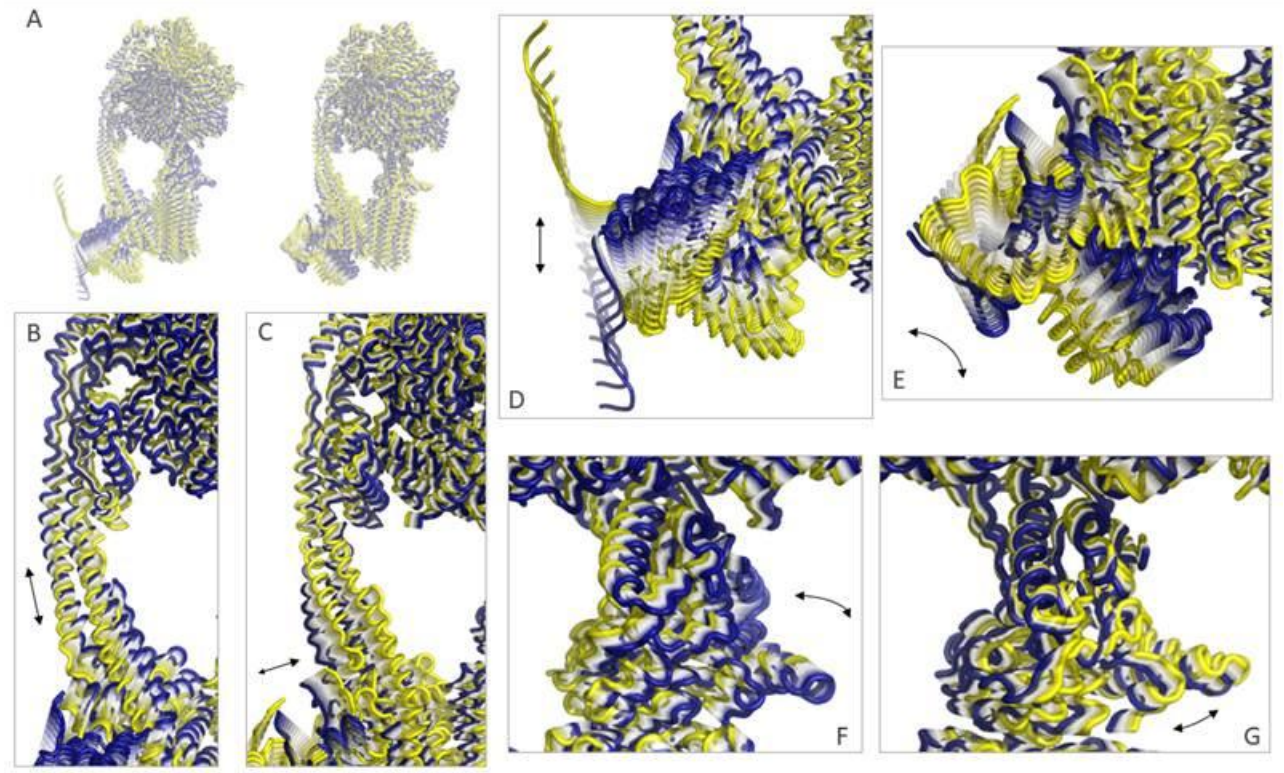

Figure 5. Normal Mode 11 analysis of WT and K45Q mutant F_1F_0-ATPase. (A) Global view of NM 11 for WT (left) and K45Q (right). **(B, C)** Detail of peripheral stalk (b subunit) oscillations in WT (B) and K45Q (C). **(D, E)** Detail of F_0 subunits e, f, and g oscillations in WT (D) and K45Q (E). **(F, G)** Detail of central stalk (γ, δ, ε) and c_8-ring movements in WT (F) and K45Q (G). Oscillations are represented by a yellow-to-blue color gradient, with arrows indicating direction. Extreme conformational states are fully opaque, while intermediate states are shown with transparency gradient. K45Q exhibits altered and less coordinated oscillations across the peripheral and central stalks and F_0 subunits, consistent with predicted reduced mechanical coupling and partial uncoupling of ATP synthesis described in the main text.

Supplementary Figures

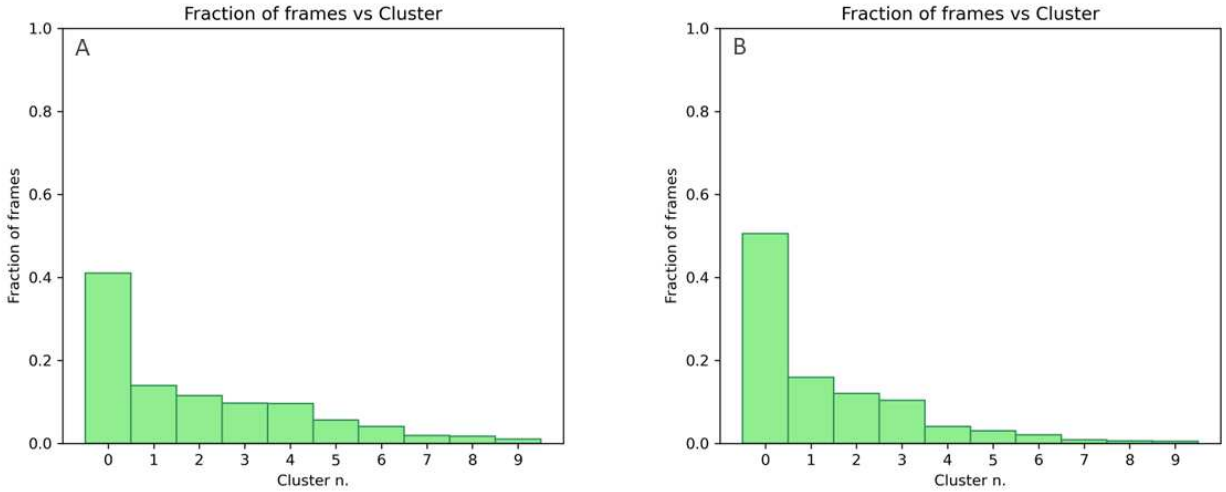

S1. Clustering of MD simulation frames for WT and K45Q ATP synthase. Fraction of frames from the full 100-ns MD trajectories assigned to clusters 0-9 for WT **(A)** and K45Q **(B)**. Clustering was performed using the average linkage algorithm, with the number of clusters set to 10. WT structures occupied cluster 0 for 41% of frames, whereas K45Q occupied the same cluster for 56.9% of frames, indicating mutation-induced conformational rearrangements and increased local flexibility. These results are consistent with the altered structural behavior and reduced coordination of K45Q described in the main text.

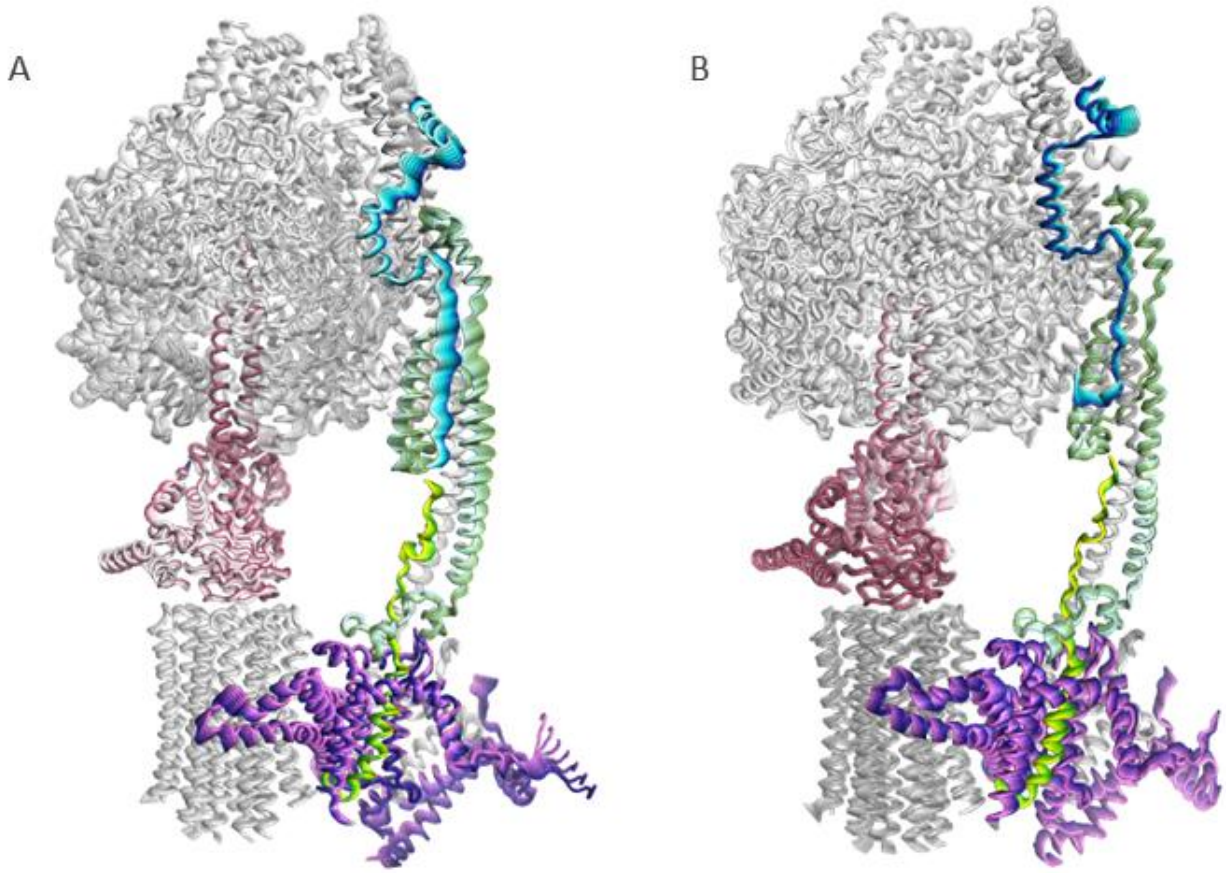

S2. PCA of MD simulations for WT and K45Q ATP synthase. Principal component 1 (PC1) is shown as a sequence of states indicating motion amplitude, color-coded from dark to light. Subunits are colored as follows: ATP8 (green-yellow), d (light green-white), F6 (blue-light blue), a, e, g, f (purple-pink), and central stalk γ, δ, ε (pink-white). PC1 captures motions associated with flexibility of the central stalk and ATP8 intramembrane region, extending to neighboring F_0 subunits. The K45Q mutant exhibits increased motion amplitude and reduced coordinated movements compared with WT, consistent with altered structural dynamics and local flexibility described in the main text.

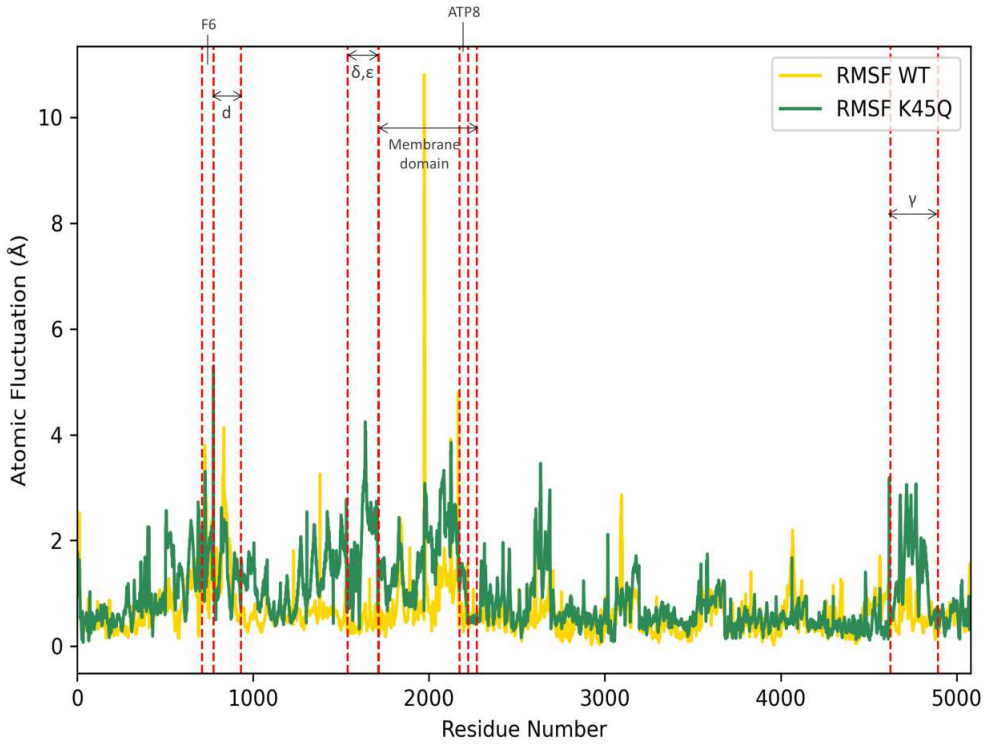

S3. RMSF analysis of WT and K45Q ATP synthase MD simulations. Per-residue Root Mean Square Fluctuation (RMSF) values along PC1 are shown, highlighting regions of the enzyme most affected by flexibility changes. The K45Q mutant exhibits increased RMSF in the central stalk, ATP8 intramembrane region, and neighboring F_0 subunits (a, e, f, g), reflecting enhanced local flexibility and reduced coordinated motions compared with WT, consistent with the altered structural dynamics described in the main text.

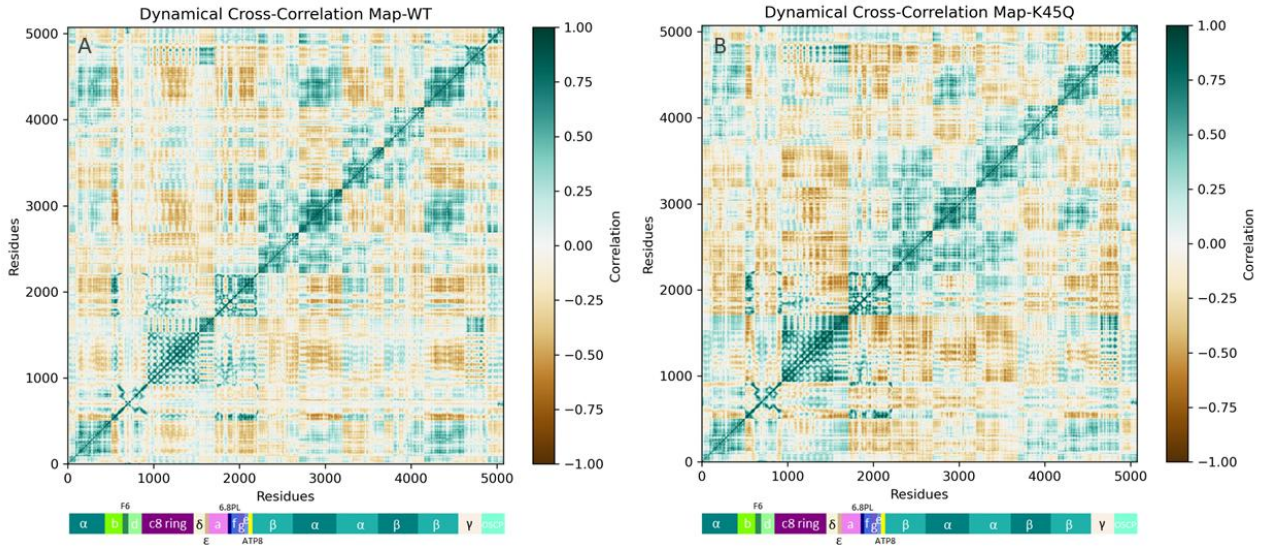

S4. Dynamical cross-correlation maps of WT and K45Q ATP synthase. Correlation maps were calculated over the 50-100 ns interval of the MD simulations for WT **(A)** and K45Q **(B)**. Positive correlations are shown in green, negative correlations in brown. In K45Q, ATP8 intramembrane residues exhibit altered correlations with F_0 subunits (a, e, f, g) and F_1 α/β chains, alongside increased anticorrelation with both central and peripheral stalks. Extramembrane ATP8 residues show higher variability, reflecting region-specific hypoflexibility and disruption of long-range coordination compared with WT, consistent with the altered structural dynamics described in the main text.

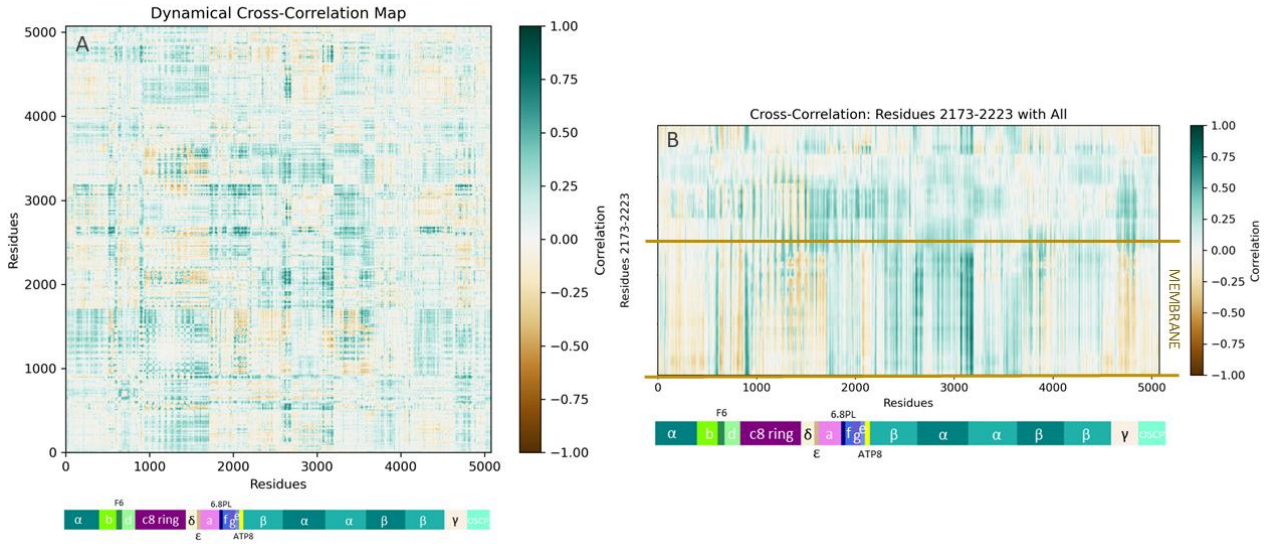

S5. Difference maps of K45Q and WT dynamical cross-correlations (DCCMs). (A) Algebraic difference across the full protein. **(B)** Focus on the ATP8 domain (residues 2173-2223), highlighting differences in correlation values (K45Q-WT). The K45Q mutant exhibits altered correlations compared with WT, with ATP8 residues showing decreased positive correlations with F_0 and F_1 subunits and increased anticorrelation with central and peripheral stalks. These changes reflect mutation-induced rewiring of collective motions and reduced coordinated dynamics, consistent with the altered structural behavior described in the main text.

2.5 Impaired Mitochondrial Respiration in osimertinib-resistant EGFR mutant NSCLC cells

To test whether the predicted ATP synthase uncoupling translates into functional bioenergetic defects, we compared mitochondrial respiration in parental and osimertinib-resistant cells using Seahorse XF real-time metabolic flux analysis. Sequential treatment with oligomycin, FCCP, and antimycin A/rotenone allowed quantification of ATP-linked respiration, proton leak, maximal respiration, and non-mitochondrial oxygen consumption.

Basal oxygen consumption rates (OCRs) were comparable between Par and OsiR cells, indicating preserved baseline respiratory activity despite chronic drug exposure. However, OsiR cells exhibited a significant reduction in ATP-linked respiration **(Figure 6)**, consistent with impaired coupling between electron transport and ATP synthesis. In line with this phenotype, proton leak was increased, reflecting compromised maintenance of the proton motive force across the inner mitochondrial membrane. In parallel, spare respiratory capacity was markedly reduced, indicating diminished ability of OsiR cells to respond to energetic stress **(Figure 6).**

To further evaluate the functional consequences of mitochondrial dysfunction, mitochondrial ROS levels were quantified using MitoSOX. H1975-OsiR cells exhibited significantly increased mitochondrial ROS levels compared with parental cells (**Suppl. Fig. S6**), consistent with the enrichment of ROS-related pathways identified by RNA-sequencing (**Figure 1**).

These results indicate that osimertinib resistance is associated with a dysfunctional, yet not fully suppressed, mitochondrial respiratory state. Rather than a global collapse of OXPHOS, resistant cells preserve basal respiration while selectively losing ATP-producing efficiency and respiratory flexibility. This respiratory profile aligns with selective remodeling of OXPHOS components observed at the genomic and structural levels, providing functional support for the mitochondrial uncoupling and bioenergetic rewiring in OsiR cells.

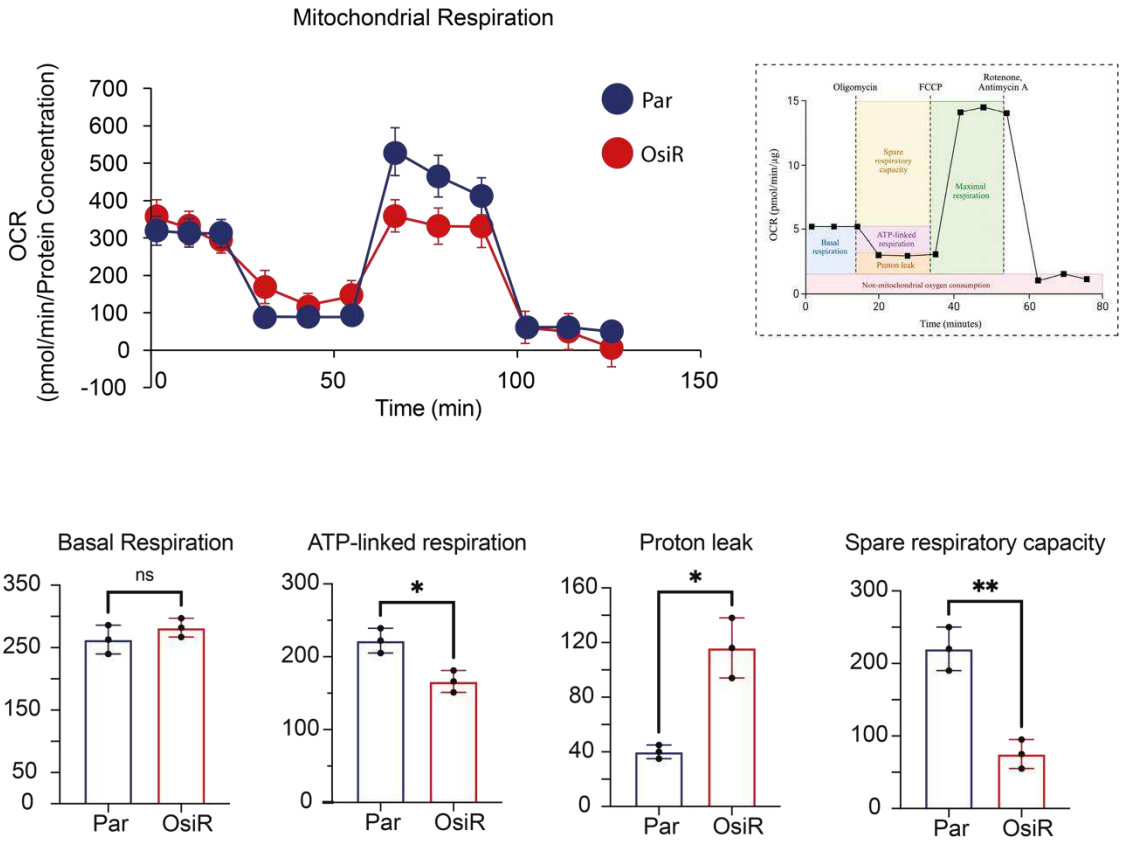

Figure 6. Seahorse analysis reveals impaired mitochondrial respiration and reduced oxidative capacity in osimertinib-resistant EGFR mutant NSCLC cells. Real-time measurement of oxygen consumption rate (OCR) in H1975 Par (red) and OsiR (black) cells using the Seahorse XF Analyzer. The top graph displays dynamic OCR profiles over time, alongside a schematic of the Mito Stress Test parameters (1.5 µM oligomycin, 2 µM FCCP, 0.5 µM rotenone/antimycin A injections). The lower panels show quantification of key mitochondrial parameters: basal respiration, ATP-linked respiration, proton leak, and spare respiratory capacity. Error bars represent standard deviation (SD); *p*-values are indicated (n=3 Par, n=3 OsiR; Welch's t-test; 0.0332 (*), 0.0021 (**), 0.0002 (***), <0.0001 (****)).

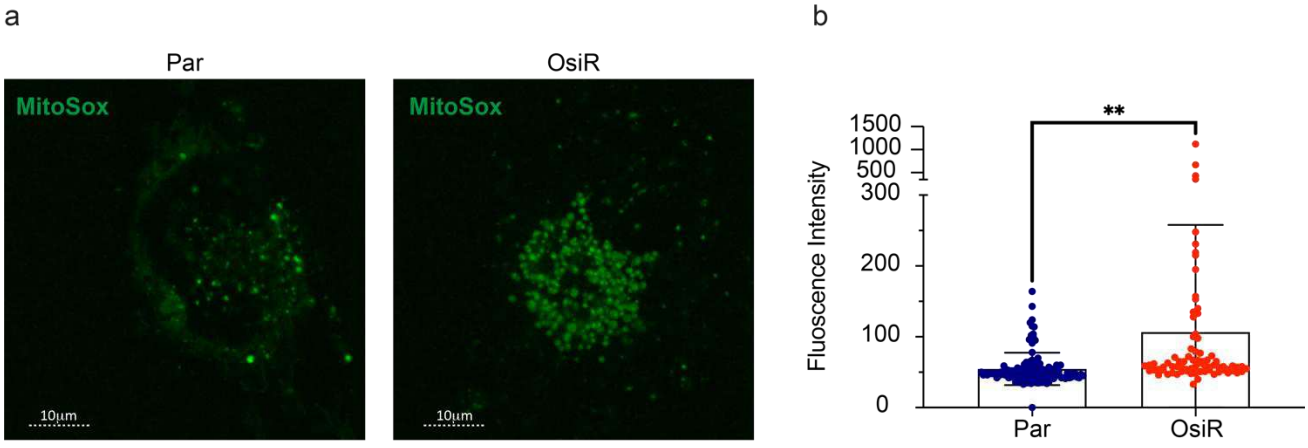

S6. Elevated mitochondrial oxidative stress in osimertinib-resistant EGFR mutant NSCLC cells. (a) Representative confocal images of H1975 Par and OsiR cells stained with MitoSOX (green), a mitochondrial superoxide indicator. Scale bar, 10 µm. **(b)** Quantification of MitoSOX fluorescence intensity in Par (blue) and OsiR (red) cells. Error bars represent standard deviation (SD); statistical significance is indicated (n=125 Par, n=77 OsiR: Welch's T test; 0.0332 (*), 0.0021 (**), 0.0002 (***), <0.0001 (****))

2.6 PAA-associated metabolic adaptation in osimertinib-resistant cells

Having established that ATP synthase dynamics are altered and mitochondrial respiratory is compromised in OsiR cells, we next examined extracellular metabolic outputs. Exometabolomic profiling of culture supernatants was

performed using complementary HPLC-DAD-FD, GC-MS, and LC-HRMS approaches. Pathway and biomarker enrichment analyses revealed dysregulation of central carbon metabolism in OsiR cells, consistent with transcriptomic signatures and altered mitochondrial bioenergetics. Specifically, metabolite patterns indicated metabolic remodeling involving glycolysis, gluconeogenesis, and the pentose phosphate pathway (PPP). Quantitative profiling revealed reduced extracellular glyceraldehyde-3-phosphate (G3P), accompanied by increased 3-phosphoglyceric acid (3-PGA), pyruvate, lactate, acetaldehyde, and acetate **(Figure 7a)**. Acetate, which was undetectable in Par cells by LC-DAD analysis and detected at lower levels than in OsiR cells in the ^{13}C-tracing experiments owing to the higher sensitivity of the GC-MS method, emerged as the predominant acidic metabolite contributing to extracellular acidification, consistent with the enhanced glycolytic transcriptomic signatures and the observed decrease in culture medium pH **(Figure 7b)**.

Western blot analysis confirmed increased expression of the glycolytic enzyme aldolase A (ALDOA) in OsiR cells **(Figure 7c)**. Transcriptomic analysis showed downregulation of oxidative PPP enzymes, including glucose-6-phosphate dehydrogenase (G6PD, -0.57; adj. p-value 0.0003) and hexose-6-phosphate dehydrogenase (H6PD, -0.81; adj. p-value 9.34E-08) **(Figure 7d)**, while the enzyme transketolase (TKT) that connects the glycolysis to the non-oxidative PPP was upregulated **(Figure 7e)**. In parallel, increased transcriptomic and protein expression of $NADP^+$-dependent aldehyde dehydrogenases, mitochondrial ALDH2 and cytosolic ALDH7A1 (**Figure 1c**), supported the conversion of acetaldehyde to acetate. Western blot validation also confirmed increased mitochondrial pyruvate dehydrogenase (PDH) (**Figure 7f**) and succinate dehydrogenase (SDH) (**Figure 3c**), indicating coordinated metabolic adaptation. Stable-isotope tracing using U-13C-glucose further revealed increased production and extracellular accumulation of glucose-derived acetate in OsiR cells, supporting enhanced routing of glucose-derived carbon toward PAA-associated metabolism (**Figure 7g**).

Additional protein analyses showed increased expression of GLUT1 and SLC16A3/MCT4, while LDHA levels remained largely unchanged (**Suppl. Fig. S7**), supporting enhanced glucose utilization and monocarboxylate transport in resistant cells.

Collectively, these data demonstrate that impaired mitochondrial efficiency in OsiR cells is accompanied by increased glycolysis, acetate accumulation, selective engagement of non-oxidative PPP enzymes, and enhanced glucose-derived acetate production, consistent with an acetate-associated metabolic adaptation in drug-resistant cells.

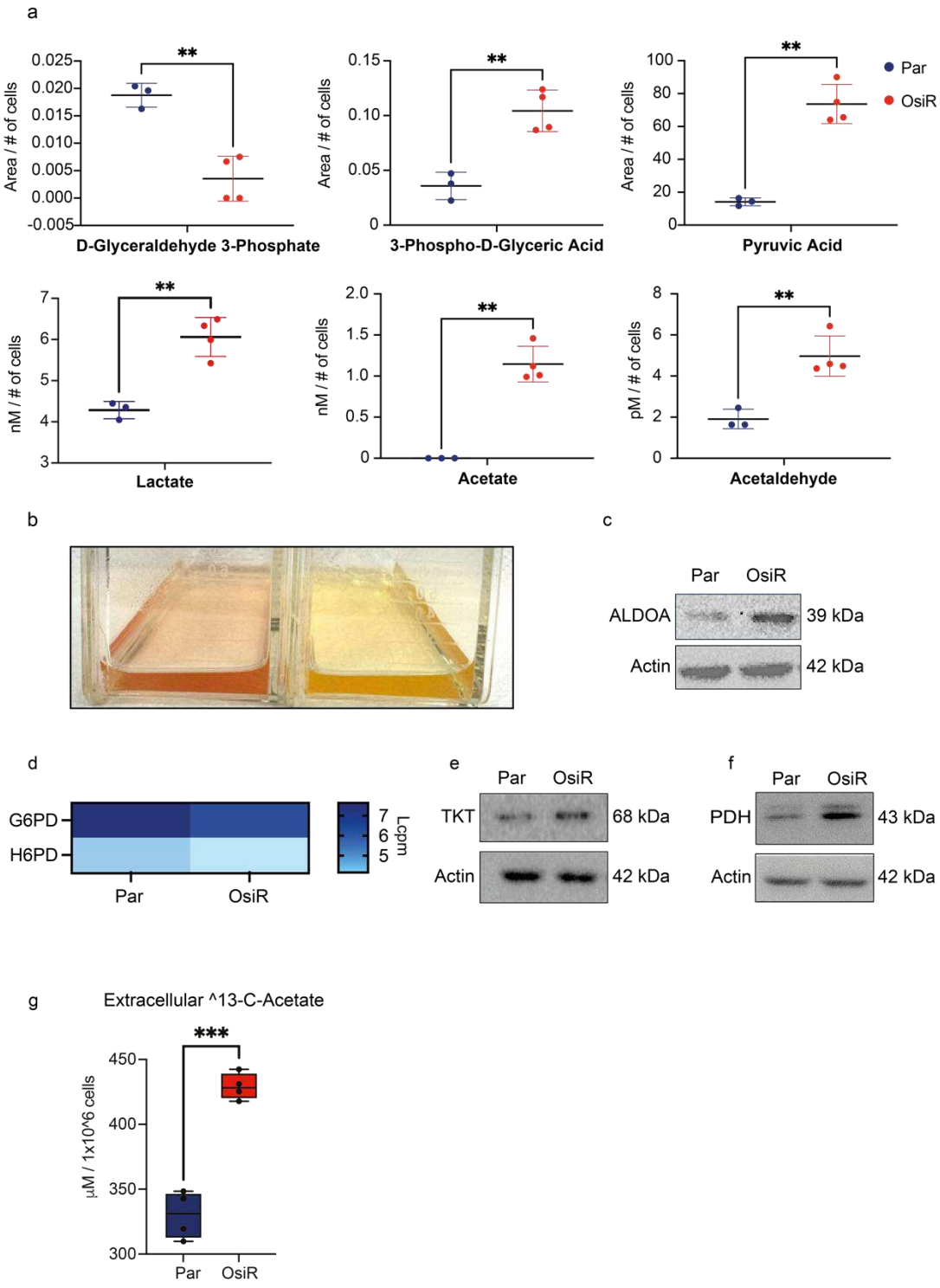

Figure 7. Exometabolomic and isotope-tracing analyses reveal acetate-associated metabolic adaptation in osimertinib-resistance in EGFR mutant NSCLC cells. (a) Exometabolomic analysis of secreted metabolites in the cell culture medium of H1975 Par (blue) and OsiR cells (red). Error bars represent standard deviation (SD); p-values are indicated (n=3 Par, n=4 OsiR; Welch's t-test; 0.0332 (*), 0.0021 (**), 0.0002 (***), <0.0001 (****)). **(b)** Representative images of the extracellular medium from H1975 OsiR (right) and Par cells (left). Yellow coloration indicates increased acidification in OsiR cells. **(c)** Western blot analyses of H1975 Par and OsiR cells. Protein lysates were immunoblotted with an anti-ALDOA antibody. Loading was assessed with an anti-β-actin antibody. Expected molecular weights (kDa) are indicated. **(d)** Heat map showing relative gene expression of G6PD and H6PD in Par and OsiR H1975 cells **(e-f)** Western blot analyses of Par and OsiR cells. Protein lysates were immunoblotted with an anti-TKT or PDH antibody. **(g)** Extracellular 13C-acetate levels (µM/1×10^6 cells) in H1975 Par and OsiR cells, measured by isotope tracing; statistics are indicated in the graph (n=2 Par, n=3 OsiR; Welch's t-test; 0.0332 (*), 0.0021 (**), 0.0002 (***), <0.0001 (****)).

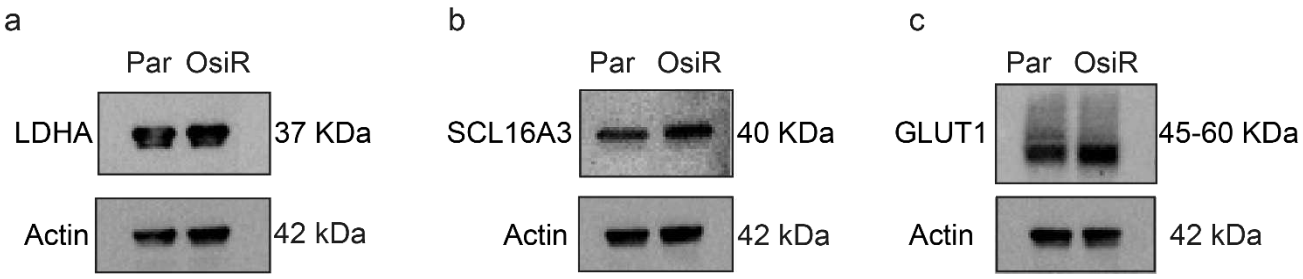

S7. Expression of glycolysis-related proteins in osimertinib-resistant EGFR-mutant NSCLC cells. (a-c) Western blot analyses of H1975 Par and OsiR cells. Protein lysates were immunoblotted with antibodies against LDHA **(a)**, SLC16A3 **(b)**, and GLUT1 **(c)**. β-actin was used as a loading control. Expected molecular weights (kDa) are indicated.

2.7 ALDH2 loss-of-function functionally links acetate-associated metabolism to osimertinib resistance

The consistent upregulation of ALDH2 at both transcript (**Figure 1b**) and protein levels (**Figure 1c**), together with the accumulation of acetate and activation of the PAA pathway, suggested that ALDH2 may represent a key functional component of the adaptive metabolic program observed in OsiR cells.

To determine whether aldehyde dehydrogenase activity contributes to osimertinib resistance, H1975-OsiR cells were treated with the ALDH inhibitor disulfiram at a sub-cytotoxic concentration of 35 nM, selected to maintain approximately 80% cell viability when administered as a single agent (**Supplementary Figure S8a**). Under these conditions, disulfiram partially restored sensitivity to osimertinib, reducing the IC50 from 2.961 µM to 1.411 µM (**Supplementary Figure S8b**).

We therefore performed CRISPR-Cas9-mediated disruption of *Aldh2* to directly assess its contribution to osimertinib resistance. Successful disruption of the *Aldh2* locus was confirmed by genomic analysis, which identified a homozygous frameshift deletion predicted to generate a truncated ALDH2 protein (66 aa versus 517 aa in the wild-type protein), and loss of ALDH2 protein expression was validated by Western blotting (**Figure 8a-e**). Functional dose-response assays showed that *Aldh2* knockout (Aldh2 KO) markedly restored osimertinib sensitivity, reducing the osimertinib IC50 from 3.019 µM in the *Aldh2* wild-type clone to 0.9805 µM in the *Aldh2* KO clone (**Figure 8f**). Consistently, *Aldh2*-deficient cells exhibited a reduced response to osimertinib challenge, with cell numbers decreasing from 83.56% in OsiR *Aldh2* WT cells to 52.82% in *Aldh2* KO cells following treatment with 1 µM osimertinib (**Figure 8g**).

We next assessed whether ALDH2 loss altered the metabolic state of resistant cells. Metabolic profiling revealed significantly increased extracellular acetaldehyde levels and unchanged acetate levels in *Aldh2*-deficient cells (**Figure 8h**). Extracellular pyruvate levels were reduced in *Aldh2* KO cells, whereas lactate levels remained unchanged (**Figure 8h**). The accumulation of acetaldehyde is consistent with impaired conversion of acetaldehyde to acetate following *Aldh2* disruption.

In parallel, *Aldh2* knockout reduced the intracellular abundance of both total NADP(H) pools, NADPH and $NADP^+$ levels (**Figure 8i**), whereas the NADP/NADPH ratio remained unchanged (**Figure 8j**).

Together, these results demonstrate that aldehyde dehydrogenase-dependent metabolism is not merely associated with the OsiR metabolic state but functionally contributes to the maintenance of osimertinib resistance.

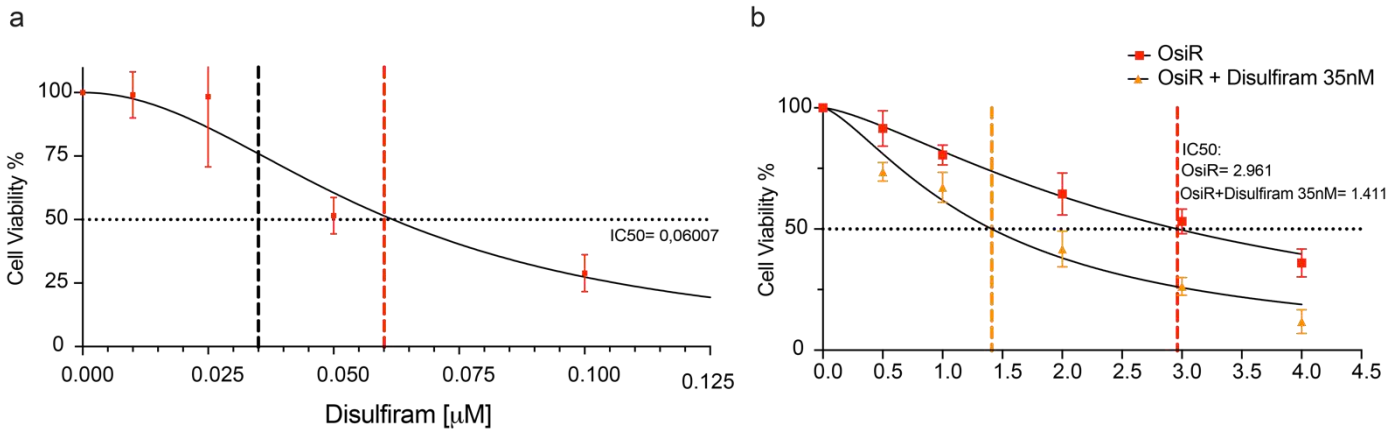

S8a-b. Disulfiram sensitizes osimertinib-resistant H1975 cells to osimertinib treatment. (a) Dose-response curve of H1975 OsiR cells treated with disulfiram (red), with the IC50 value indicated. **(b)** Dose-response curves of H1975 OsiR cells treated with osimertinib alone (red) or in combination with disulfiram (orange; 35 nM).

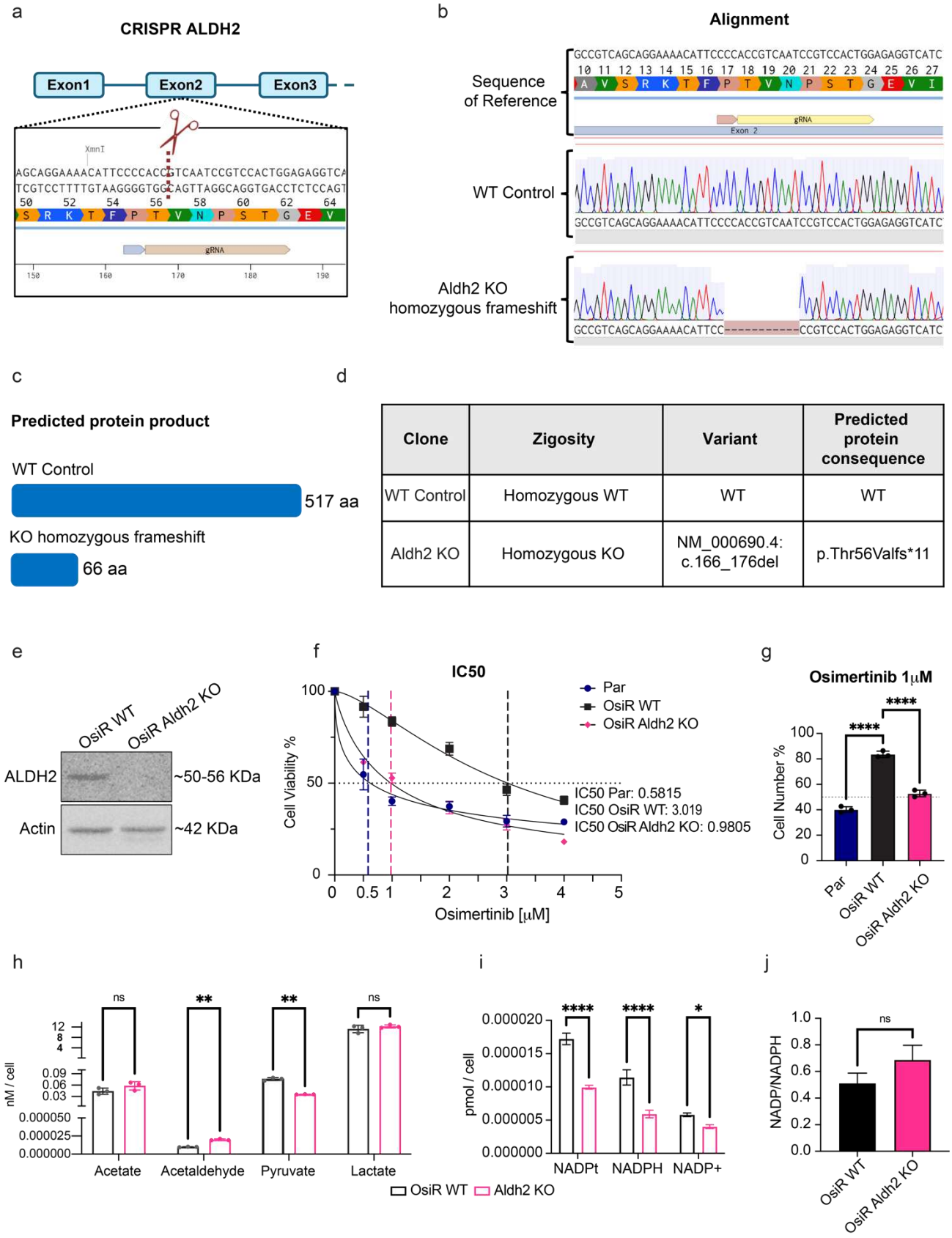

Clone	Zigosity	Variant	Predicted protein consequence
WT Control	Homozygous WT	WT	WT
Aldh2 KO	Homozygous KO	NM_000690.4: c.166_176del	p.Thr56Valfs*11

Figure 8. CRISPR-Cas9 knockout of *Aldh2* restores osimertinib sensitivity in resistant H1975 cells. (a) Schematic of CRISPR-Cas9 targeting strategy for *Aldh2*, showing gRNA position within Exon 2 and predicted Cas9 cut site. **(b)** Sanger sequencing alignment of reference sequence, WT control cell clone, and *Aldh2* homozygous knockout (KO) cell clone. **(c)** Predicted protein product length for WT (517 aa) versus Aldh2 KO homozygous frameshift (66 aa).

(d) Clone zygosity, variant nomenclature, and predicted protein consequence for WT control and Aldh2 KO clones. **(e)** Western blot analysis of OsiR WT and OsiR Aldh2 KO cells. Protein lysates were immunoblotted with an anti-ALDH2 antibody. Loading was assessed with an anti-β-actin antibody. Expected molecular weights (kDa) are indicated. **(f)** Osimertinib dose-response curves and IC50 values in Par (blue), OsiR WT (black), and OsiR Aldh2 KO (magenta) cells, after 1 μM osimertinib treatment. n=3 per group; one-way ANOVA; p-values correspond to 0.0332 (*), 0.0021 (**), 0.0002 (***), <0.0001 (****). **(g)** Cell number (%) after osimertinib treatment in Par (blue), OsiR WT (black), and OsiR Aldh2 KO (magenta) cells. n=3 per group; one-way ANOVA; p-values correspond to 0.0332 (*), 0.0021 (**), 0.0002 (***), <0.0001 (****). **(h)** Acetate, acetaldehyde, pyruvate, and lactate levels (nM/cell) in OsiR WT (in black) versus Aldh2 KO (magenta) cells. n=3 per group; Welch's t-test; p-values correspond to 0.0332 (*), 0.0021 (**), 0.0002 (***), <0.0001 (****). **(i)** NADPt, NADPH and NADP+ levels (pmol/cell) in OsiR WT (black) versus Aldh2 KO (magenta) cells. n=2 WT, n=3 Aldh2 KO; 2way Anova p-values correspond to 0.0332 (*), 0.0021 (**), 0.0002 (***), <0.0001 (****). **(j)** NADP/NADPH ratio in OsiR WT (black) versus Aldh2 KO (magenta) cells. n=2 WT, n=3 Aldh2 KO; Welch's t-test; ns, not significant.

2.8 *In vivo* validation of mitochondrial inefficiency and PAA-associated metabolic rewiring in osimertinib-resistant EGFR^{LT} tumors

Having established that ALDH2-associated metabolism functionally contributes to osimertinib resistance *in vitro*, we next asked whether related mitochondrial and PAA-associated signatures were also detectable *in vivo*. To address this question, we performed single-cell RNA sequencing of EGFR^{LT} mouse lung tumors carrying the same EGFR mutation set as H1975 cells. Tumors were collected under vehicle treatment, during osimertinib response, and after acquisition of resistance, enabling assessment of tumor cell states under therapeutic pressure.

UMAP analysis identified a pulmonary population of tumor-derived Alveolar Type 2 (AT2)-like cells, characterized by *Stpc* expression (**Figure 9a**). These cells primarily mapped to clusters 2, 14, 16, and 21 (**Figure 9b**). Their frequency decreased during the osimertinib-responsive phase and increased upon acquisition of resistance (**Figure 9c, Suppl. Table 3**), indicating that tumor-derived AT2-like cells persist and expand in resistant tumors.

In line with the metabolic phenotype observed *in vitro*, AT2-like cells from osimertinib-resistant EGFR^{LT} tumors displayed upregulation of genes involved in glycolysis, mitochondrial metabolism, and PAA-associated pathways, including *Ldh*, *Aldh2*, *Aldh7a1*, *AldoB*, *Pdha*, *Tkt*, and multiple subunits of mitochondrial Complex II (*Sdha*, *Sdhb*, *Sdhc*, *Sdhd*) (**Figure 9d**). EnrichR analysis comparing resistant and -sensitive AT2-like clusters revealed a pronounced enrichment of mitochondrial pathways in all the AT2-like resistant clusters relative to their sensitive counterpart (**Supplementary Data 3**), mirroring the transcriptional signatures observed *in vitro*. Enriched categories included mitochondrial-related WikiPathways (**Figure 9e**), the MsigDB Hallmark Oxidative Phosphorylation gene set (**Figure 9f**), and Gene Ontology terms associated with mitochondrial Biological Processes (mitochondrial gene expression, electron transport, cellular respiration) and Cellular Components (mitochondrial inner membrane, respiratory chain complex) (**Figure 9g**) and (**Figure 9h**).

Overall, these *in vivo* data confirm that mitochondrial remodeling and PAA-associated metabolic rewiring observed in OsiR H1975 cells are recapitulated in tumor-derived AT2-like cells *in vivo*, representing a core, selection-driven adaptive trait of osimertinib-resistant tumors.

Supplementary Table 3. Percentage distribution of the different clusters identified within the dataset.

Cluster #	Tumor_VHL	Tumor_OsiS	Tumor_OsiR
1	34.5	28.1	37.4
2	34.4	25.2	40.5
3	18.6	28.3	53
4	31	35.4	33.6
5	18.9	27.8	53.3
6	30.1	20	49.9
7	38.6	24.1	37.4
8	35.3	25.6	39.1
9	35.6	24.3	40.2
10	20.1	27.8	52.1
11	18	31.2	50.8
12	27.6	14.6	57.8

13	19.6	28	52.4
14	22.6	3.7	73.6
15	52.7	10.2	37
16	37.3	6.3	56.4
17	11.2	23.4	65.4
18	24.4	14.5	61.1
19	18	28.9	53.1
20	12.8	22.8	64.4
21	41.4	26.1	32.5
22	9.1	33.9	57
23	17.7	28.5	53.8
24	8.6	27.3	64.1
25	15.6	27.1	57.3
26	13.2	24.6	62.2
27	25.2	15.3	59.5
28	30	20.7	49.3
29	6.8	37.4	55.8

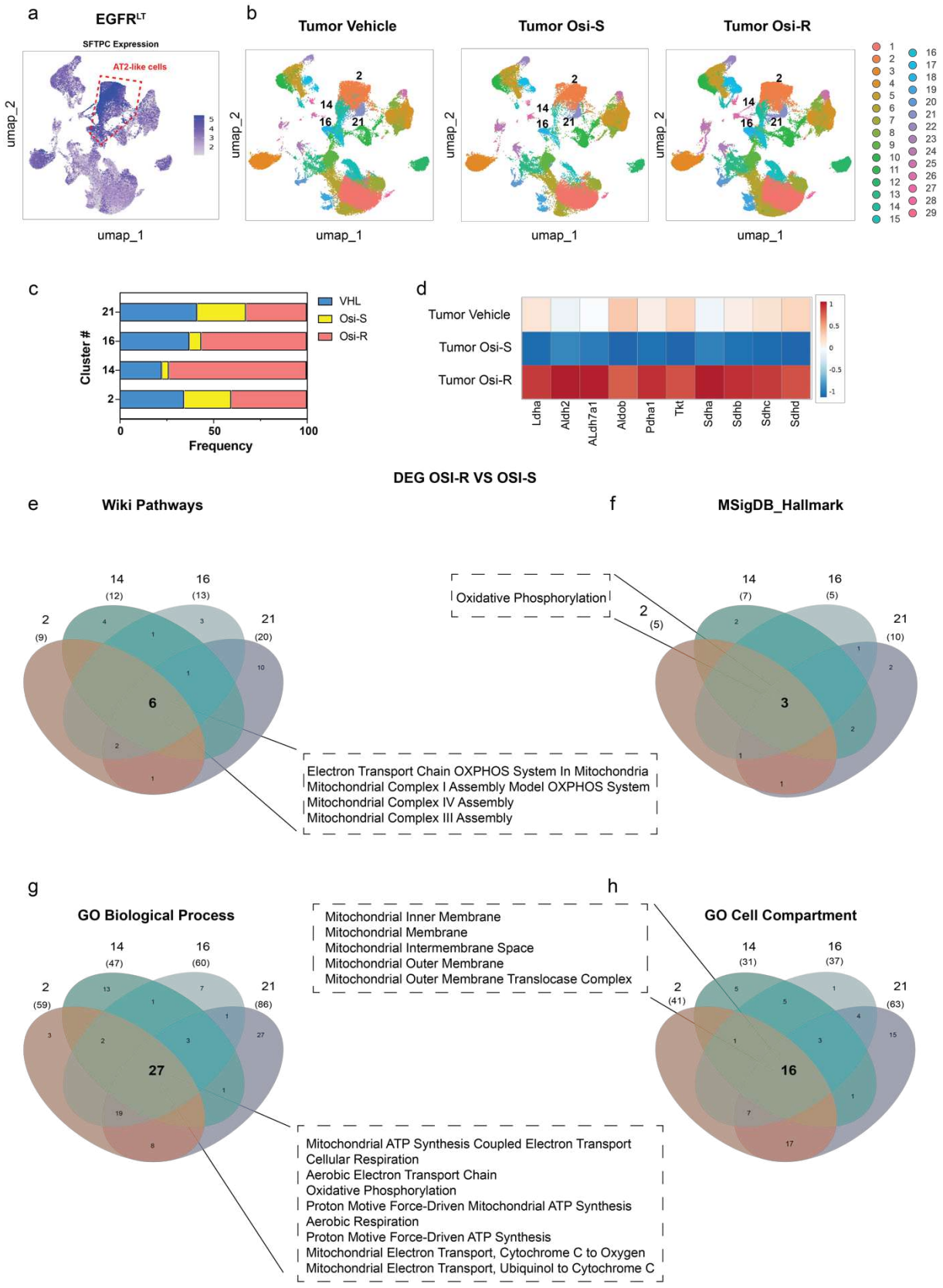

Figure 9: scRNAseq data of EGFR^{LT} tumors confirms mitochondrial alteration in osimertinib resistant AT2-like tumor cells. a) UMAP plot showing *Sftpc* expression within the dataset to highlight AT2-like cells. **b)** UMAP plots showing cluster distribution in EGFR^{LT} tumors upon vehicle treatment (VHL), during osimertinib response (OsiS), and after acquisition of resistance (OsiR). **c)** Frequency of AT-2 like clusters (*Sftpc*-positive) in VHL, OsiS and OsiR tumors. **d)** Heatmap showing z-score of selected PAA-related genes by condition. **e-h)** Venn diagram showing enrichment of mitochondrial-related pathways in resistant versus sensitive AT2-like clusters following differential gene expression (DGE) and subsequent EnrichR pathway analysis. Enriched categories include Wiki pathways **(e)**, MSigDB_Hallmark **(f)**, and Gene Ontology (GO) categories within Biological Process **(g)** and Cell Compartment **(h)**.

DISCUSSION

Resistance to EGFR-targeted tyrosine kinase inhibitors (TKIs) remains a major clinical barrier in NSCLC. Although osimertinib is the standard of care for EGFR-mutant patients, its clinical efficacy is ultimately limited by acquired resistance. Established mechanisms include secondary mutations, lineage plasticity, and epigenetic reprogramming, yet the contribution of mitochondrial adaptation to resistance has remained largely unexplored.

Here, we uncover a mitochondria-associated adaptive dimension of osimertinib resistance, integrating structural, genetic, and metabolic reprogramming. Resistant cells exhibit remodeled mitochondrial networks, impaired OXPHOS, and reduced spare respiratory capacity, reflecting a stress-adapted bioenergetic state. Despite these functional limitations, mitochondria remain metabolically active, orchestrating a rewiring program that supports survival under therapeutic stress, maintains anabolic processes, and contributes to metabolic and redox adaptation. Altogether, these features define a dysfunctional yet paradoxically supportive mitochondrial state. Rather than representing a simple loss of mitochondrial function, these alterations appear to be accompanied by metabolic rewiring that enables resistant cells to adapt to energetic and therapeutic stress. The MT-ATP8 K45Q variant identified in resistant cells may contribute to altered ATP synthase function; however, given its low allele frequency and non-homoplasmic status, we consider it a potential component of the resistant phenotype rather than a demonstrated driver of resistance.

Single-cell transcriptomic profiling of osimertinib-resistant $EGFR^{LT}$ tumors largely recapitulated the mitochondrial and metabolic phenotypes observed *in vitro*. The affected population consisted of AT2-like tumor epithelial cells, which persist and expand upon acquisition of resistance. Resistant AT2-like clusters exhibited upregulation of mitochondrial, glycolytic, and PAA-associated pathways, indicating that mitochondrial remodeling represents a selection-driven trait under drug pressure. Importantly, these tumors harbored the same EGFR mutation set as H1975 cells, supporting the biological relevance of the metabolic framework defined *in vitro*. The enrichment of mitochondrial and PAA pathway-associated transcriptional programs in resistant AT2-like cells further supports the presence of this metabolic adaptation in the tumor context, although these *in vivo* data remain correlative and do not by themselves establish a causal role in *in vivo* resistance.

A major finding of this study is the identification of a metabolic program centered on the pyruvate-acetaldehyde-acetate pathway in H1975-OsiR cells. Resistant cells display increased extracellular pyruvate, lactate, acetaldehyde, and acetate, together with altered expression of enzymes involved in aldehyde metabolism and remodeling of the pentose phosphate pathway. U-^{13}C-glucose tracing further demonstrated increased accumulation of glucose-derived acetate in the extracellular compartment, providing direct evidence that glucose-derived carbon contributes to the acetate pool in resistant cells. These findings support metabolic redistribution toward acetate production, while not necessarily establishing a complete linear flux through every intermediate of the PAA pathway. This remodeling is accompanied by increased GLUT1 and MCT4 expression, consistent with altered glucose uptake and monocarboxylate transport, whereas LDHA expression remains largely unchanged, suggesting that the phenotype reflects broader carbon metabolic rewiring rather than simply increased lactate production.

Importantly, our data provide functional evidence linking aldehyde metabolism to osimertinib resistance. Pharmacological ALDH inhibition with disulfiram reduced the osimertinib IC50 from 2.961 μM to 1.411 μM, while CRISPR-Cas9-mediated ALDH2 knockout reduced the IC50 from 3.019 μM to 0.9805 μM. ALDH2 loss also increased extracellular acetaldehyde without a corresponding increase in acetate, consistent with impaired acetaldehyde conversion, and was accompanied by reduced extracellular pyruvate levels, whereas lactate levels remained unchanged. Together, these complementary pharmacological and genetic approaches indicate that aldehyde dehydrogenase-dependent metabolism is not merely a correlate of resistance but contributes functionally to maintenance of the resistant phenotype.

The contribution of ALDH2-associated metabolism to redox homeostasis appears to extend beyond regulation of the $NADPH/NADP^+$ balance. ALDH2 knockout reduced both $NADP^+$ and NADPH pools, whereas the $NADPH/NADP^+$ ratio remained unchanged. Thus, the contribution of ALDH2 to osimertinib resistance cannot be explained solely by maintenance of the global $NADPH/NADP^+$ ratio. Instead, ALDH2 activity may contribute to broader pyridine nucleotide and metabolic homeostasis, allowing resistant cells to maintain metabolic flexibility under conditions of

mitochondrial dysfunction and altered PPP activity. This interpretation is consistent with the remodeling of the PPP observed in H1975-OsiR cells and supports a model in which mitochondrial, aldehyde-metabolic, and PPP-associated adaptations cooperate to sustain the resistant state.

Collectively, these findings support a model in which mitochondrial remodeling and metabolic rewiring constitute interconnected adaptive components of acquired osimertinib resistance. Rather than acting as passive consequences of mitochondrial dysfunction, acetate-associated metabolism and ALDH2 activity contribute functionally to maintenance of the resistant phenotype.

Importantly, we do not propose this metabolic program as a universal mechanism of EGFR-mutant NSCLC resistance. Our findings support the existence of a context-dependent adaptive state identified in the H1975-OsiR model and recapitulated in resistant EGFRL858R/T790M tumor-derived AT2-like cells.

From a therapeutic perspective, the functional dependence on ALDH2-associated metabolism identifies aldehyde metabolism as a potential metabolic vulnerability that may be exploited to enhance osimertinib sensitivity. Future studies will be required to determine the prevalence of this adaptation in additional resistant models and to evaluate whether pharmacological targeting of ALDH-dependent pathways can be effectively combined with EGFR inhibition.

MATERIAL AND METHODS

Cell culture conditions: The parental human lung cancer cell line H1975, which harbors the *EGFR L858R/T790M* mutation, was obtained from ATCC. The osimertinib-resistant variant was generated by gradually exposing parental H1975 cells to increasing concentrations of osimertinib, up to a final concentration of 1 μM, at which the cells remained viable. Cells were maintained in RPMI-1640 medium supplemented with 10% fetal bovine serum (FBS), 1% L-glutamine, and 1% penicillin/streptomycin, at 37°C in a humidified incubator with 5% CO2.

Total RNA Sequencing: Total RNA was extracted from both H1975-Par and -OsiR cells using the RNeasy Plus Mini Kit (QIAGEN#74134, Hilden, Germany), following the manufacturer's instructions. RNA concentration and integrity were evaluated using a NanoDrop 2000 spectrophotometer (Thermo Fisher Scientific, Waltham, MA, USA). RNA sequencing was performed by IGATech (IGA Technology Services, Udine, Italy). RNA libraries were prepared using the Universal Plus mRNASeq kit (Tecan Genomics, Redwood City, CA, USA), following the protocol for *fr-secondstrand* libraries. RNA quality was evaluated using either the Agilent 2100 Bioanalyzer RNA assay (Agilent Technologies, Santa Clara, CA, USA) or Caliper LabChip GX system (PerkinElmer, Waltham, MA, USA). Final libraries were quantified with a Qubit 2.0 Fluorometer (Invitrogen, Carlsbad, CA, USA) and their quality was verified using the Agilent Bioanalyzer DNA assay or Caliper. Sequencing was performed using an Illumina NovaSeq 6000 platform (San Diego, CA, USA) using paired-end 150 bp reads. Read counts (in millions) per sample were as follows:
P1: 120.08
P2: 116.47
P3: 114.88
OR1: 120.35
OR2: 115.34
OR3: 103.65
Base calling, demultiplexing, and adapter masking were performed using Illumina BCL Convert v3.9.31. Adapter sequences were masked during demultiplexing, with masked bases converted to "N" characters and associated quality scores overwritten to a value of 2 to facilitate compatibility with standard trimming and quality filtering tools.

RNA sequencing reads alignment and count: RNA sequencing reads were aligned to the genome assembly GRCh38p14 using the aligner STAR[34], resulting in a mean of uniquely mapped reads per sample of 92.4% (SD 2.5%). Mapped reads were counted using featureCounts [35] and annotation file "Homo_sapiens.GRCh38.110.gtf" from Ensembl (https://www.ensembl.org), resulting in a mean of assigned reads per sample of 90.8% (SD 0.2%). The

genes-by-samples count matrix was filtered to keep only genes with at least 3 counts per million (cpm) in 3 samples, a constraint fulfilled by 11.298 genes.

Differential Gene Expression Analysis : Samples were normalized using the TMM (trimmed mean of M values) method [36] available in the R package edgeR [37]. Differential gene expression (DGE) analysis between H1975-Par and H1975-OsiR cells was performed using limma [38]. Genes with an absolute log fold change (|LogFC|) ≥ 0.25 and a false discovery rate (FDR) ≤ 0.05 were considered significantly differentially expressed.

Enrichment Analysis: The list of significantly upregulated genes was analyzed using the EnrichR platform for functional enrichment [39-41]. Enrichment analysis was performed across multiple databases, including Gene Ontology (GO) categories, Biological Processes (BP) and Cellular Components (CC), as well as Hallmark (HM) and WikiPathway (WP), to identify overrepresented biological pathways and cellular functions.

Cell Collection and Protein Extraction: H1975 Par and OsiR cells were detached from culture plates using trypsin-EDTA, centrifuged at 261x g for 5 min at room temperature, and washed with PBS. The resulting cell pellet was snap-frozen in liquid nitrogen and stored at -80°C until further processing. To extract proteins, the cell pellet was lysed for 30 minutes in 1X Triton X-100 (Thermo Scientific, #A16046) supplemented with cOmplete™ EDTA-free Protease Inhibitor Cocktail and PhosStop Phosphatase Inhibitor Cocktail (Roche, Basel, Switzerland).. The lysates were incubated on ice for 30 minutes with vortexing every 10 minutes. After incubation, the samples were centrifuged at 12,000 × g for 20 min at 4°C, and the supernatant was collected and stored at -80°C.

SDS-PAGE and Western Blotting: For protein analysis, 15 µg of protein per sample (Par and OsiR cells) was separated by SDS-PAGE on a 10% polyacrylamide gel and transferred to nitrocellulose membranes using the TransBlot Transfer System (Bio-Rad, Hercules, CA, USA). Membranes were blocked for 1 hour at room temperature in 5% non-fat dry milk or 5% bovine serum albumin (BSA) diluted in Tris-buffered saline with 0.1% Tween-20 (1X TBS-T). Primary antibodies (listed below) were incubated overnight at 4°C. After incubation, membranes were washed three times for 10 min each with 1X TBS-T at room temperature. HRP-conjugated secondary antibodies (listed below) were then applied for 1 hour at room temperature. Protein bands were detected by chemiluminescence (Pierce ECL Western Blotting Substrate Cat #32106) and visualized using the Chemidoc Imaging System (Bio-Rad). Membranes were subsequently stripped using Stripping Buffer Solution (Himedia, #ML163), as per the manufacturer's instructions, and re-probed with an anti-β-actin mouse antibody to verify equal protein loading. After three washes with 1X TBS-T, membranes were incubated with the appropriate anti-mouse secondary antibody (details below).

ANTIBODIES AND DILUTIONS	
Primary Antibody	**Dilution**
anti-β-actin mouse antibody (Santa Cruz #47778)	1/1000 (in 5% non-fat milk)
anti-ALDOA rabbit antibody (Antibodies.com #A97723)	1/1000 (in 5% non-fat milk)
anti-ALDH2 rabbit antibody (Antibodies.com #A13393)	1/1000 (in 5% non-fat milk)
anti-TKT rabbit antibody (Antibodies.com #A15167)	1/1000 (in 5% non-fat milk)
anti-ALDH7A1 rabbit antibody (Thermo Fisher Scientific #PA5-29974)	1/1000 (in 5% non-fat milk)
anti-MFN2 rabbit antibody (Cell Signaling Technology #9482)	1/1000 (in 5% non-fat milk)
anti-DRP1 rabbit antibody (Cell Signaling Technology #8570)	1/1000 (in 5% BSA)
anti-COX IV rabbit antibody (Cell Signaling Technology #4850)	1/1000 (in 5% BSA)
anti-CytC rabbit antibody (Cell Signaling Technology #4280)	1/1000 (in 5% non-fat milk)
anti-PHB1 rabbit antibody (Cell Signaling Technology #2426)	1/1000 (in 5% BSA)
anti-PDHA1 rabbit antibody (Cell Signaling Technology #3205)	1/1000 (in 5% BSA)
anti-SDHA rabbit antibody (Cell Signaling Technology #11998)	1/1000 (in 5% BSA)
anti-VDAC rabbit (Cell Signaling Technology #4661)	1/1000 (in 5% BSA)
anti-LDHA rabbit antibody (Cell Signaling Technology #71368	1/1000 (in 5% BSA)
anti-SCL16A3 rabbit antibody (Cell Signaling Technology #81569)	1/1000 (in 5% BSA)
anti-Glut1 rabbit antibody (Cell Signaling Technology #73015)	1/1000 (in 5% BSA)
Secondary Antibody	**Dilution**

anti-mouse (Immunoreagents #CkxMu-003-DHRPX)	1/2000 (in 5% non-fat milk)
anti-rabbit (Cell Signaling Technologies #7074)	1/2000 (in 5% non-fat milk)

Mitochondrial Staining and Imaging: Mitochondrial staining was performed using the MITO-ID Red Detection Kit (Enzo Life Sciences, Cat # ENZ-51007) according to the manufacturer's protocol. Confocal imaging of stained cell samples was carried out using a Zeiss LSM 900 Airyscan2 (Carl Zeiss, Jena, Germany). A 63x Apochromat oil-immersion objective (NA = 1.4) was employed, and the pinhole aperture of the confocal system was set at 1 airy unit. The excitation wavelength was set to 561 nm, and emission was detected in the 565-625 nm range. Image stacks were acquired at a resolution of 1596 × 1596 pixels^2, corresponding to a field of view of 78.0 × 78.0 µm^2, with an axial step of 0.17 µm. Four averages were taken per line scan to ensure signal clarity. The Airyscan system provides an optical lateral resolution of approximately 120 nm and an axial resolution of about 350 nm, enabling precise visualization of mitochondrial morphology. In parallel, mitochondrial superoxide levels were assessed using the MitoSOX™ Green Mitochondrial Superoxide Indicator (Invitrogen, #M36006), according to the manufacturer's instructions. Cells were incubated with the working solution for 30 minutes at 37°C and 5% CO_2, imaged in 2D (excitation/emission 488/510 nm) within 2 hours of staining, and fluorescence intensity was quantified on a per-cell basis.

Image Analysis: 3D mitochondrial reconstruction was performed by Airyscan confocal microscopy. Image processing was performed using the *Mitochondria Analyzer* plugin [42] integrated into the open-source software Fiji (NIH, Bethesda, MD, USA). The pipeline enables 3D analysis, allowing for detailed quantification of mitochondrial morphology across multiple optical planes. The following morphological parameters were assessed: Mitochondrial number per cell, Mean mitochondrial volume, Mean mitochondrial surface area, Mitochondrial sphericity, Number of branches per mitochondrion, Total branch length per mitochondrion, Branch junctions per mitochondrion and Branch end-points per mitochondrion.

Mitochondria Isolation and Extraction of Mitochondrial DNA (mtDNA) for Sequencing: Mitochondria were isolated from both H1975-Par and H1975-OsiR cells using the Qproteome Mitochondrial Isolation Kit (QIAGEN#37612), according to the manufacturer's instructions. Mitochondrial DNA (mtDNA) was then extracted from the isolated mitochondria employing the DNA Micro kit (QIAGEN#56304) by following manufacturer's instructions. mtDNA concentration and purity were assessed using the DS-11 spectrophotometer (DeNovix), the Quant-iT™ dsDNA High Sensitivity Assay Kit (Thermo Fisher Scientific), and capillary electrophoresis (Fragment Analyzer, Agilent Technologies) to ensure DNA integrity. A total of 300 ng of high-quality mtDNA was sheared to a target size range of 7-12 kb and used for library preparation with the SMRTbell Express Template Prep Kit v3.0 (PacBio), according to the manufacturer's instructions. Library preparation included DNA damage repair, end repair with A-tailing, and ligation of barcoded SMRTbell adapters. The resulting libraries were purified using SMRTbell cleanup beads (PacBio), and size and concentration were re-evaluated using capillary electrophoresis and fluorometric assays. SMRTbell libraries were pooled by equal mass and submitted to high-throughput sequencing at the Genesupport SA facility (Plan-les-Ouates, CH). Sequencing was performed by Fasteris (Genesupport SA Life Sciences, Switzerland) on the PacBio Sequel IIe platform, using the Sequel Sequencing Kit 3.0 with 1800-minute movies, and primary analysis, HiFi read generation, and demultiplexing were performed using SMRT Link Software v11.0.

Mitochondrial DNA sequencing, variant call and annotation: mtDNA sequencing was performed using the PacBio HiFi platform to ensure high-fidelity detection of single nucleotide variants and structural alterations. Long-reads from Par and OsiR samples were aligned to the Revised Cambridge Reference Sequence (rCRS) of the Human Mitochondrial DNA (GenBank sequence "NC_012920") using pbmm2 (https://github.com/PacificBiosciences/pbmm2), a PacBio-optimized wrapper for the *minimap2* aligner [43]. Variant calling was performed using MutServe2 [44]. The analysis detected a total of 2662 SNVs in Par cells and 2416 SNVs in OsiR cells. Variants were annotated using Ensembl Variant Effect Predictor (VEP, https://www.ensembl.org/Tools/VEP). Only variants with allele frequency (AF) ≥ 0.01 (in Par or OsiR cells), AF fold change (OsiR/Par and Par/OsiR) ≥ 1.5, and classified by VEP IMPACT as MODIFIER or MODERATE or HIGH were kept. This analysis led to a total of 171 variants in genes that encode mitochondrial respiratory chain complexes (annotation from MitoCarta3.0[45] **(Supplementary Data 1)**.

Genomic DNA extraction and whole genome sequencing: Total DNA was extracted from H1975-Par and H1975-OsiR cells using the DNA Micro Kit (QIAGEN, #56304), according to the manufacturer's instructions. DNA concentration and purity were assessed by spectrophotometry using a NanoDrop 2000 (Thermo Fisher Scientific). Genomic DNA was used for whole genome sequencing (WGS), which was performed by IGATech (IGA Technology Services, Italy). Libraries were prepared using the Celero™ DNA-Seq kit (NuGEN, San Carlos, CA, USA) for high-quality genomic DNA, following the manufacturer's instructions. Final libraries were quantified using a Qubit 2.0 Fluorometer (Invitrogen, Carlsbad, CA, USA) and quality-checked with the Agilent 2100 Bioanalyzer High Sensitivity DNA assay (Agilent Technologies, Santa Clara, CA, USA) to assess fragment size distribution and concentration, ensuring suitability for sequencing. Sequencing was performed on a NovaSeq 6000 platform (Illumina) in paired-end 150 bp mode. Approximately 90 Gbp of data were obtained per sample, corresponding to ~30X coverage of the human genome. Base calling, demultiplexing, and adapter masking were performed using BCL Convert v3.9.3.

Whole genome sequencing reads alignment, variant call and annotation: DNA sequencing reads alignment was performed with BWA-MEM (https://bio-bwa.sourceforge.net) against the human assembly GRCh38p14. Aligned reads were analyzed with GATK (cleaning, reordering, sorting, fixing mate information, marking duplicates and base recalibration) [46]. Mutations in OsiR vs Par, and in Par vs OsiR, were called using GATK Mutect2 and filtered using GATK "FilterMutectCalls". Variants were annotated using Ensembl Variant Effect Predictor (VEP, https:/www.ensembl.org/Tools/VEP). Only variants classified by VEP IMPACT as MODIFIER or MODERATE or HIGH were kept. This analysis led to a total of 121 variants in nuclear genes that encode mitochondrial respiratory chain complexes (annotation from MitoCarta3.0 [45]) **(Supplementary Data 2)**.

Seahorse Metabolic Flux Analysis: Real-time metabolic flux analysis was performed using the XFe96 Extracellular Flux Analyzer (Agilent/Seahorse Bioscience). H1975P and OsiR cells were seeded in Seahorse XF96 cell culture plates at a density of 15,000 cells per well. Prior to the assay, cells were washed and incubated in Seahorse XF Base Medium supplemented with 10 mM glucose, 1 mM pyruvate, and 2 mM L-glutamine. Plates were maintained in a non-CO_2 incubator at 37°C for 1 hour prior to allow temperature and pH equilibration. Oxygen consumption rates (OCRs) were measured under basal conditions and after sequential injection of mitochondrial inhibitors, following the manufacturer's instructions. Final inhibitor concentrations were 1.5 µM oligomycin, 2 µM carbonyl cyanide-p-trifluoromethoxyphenylhydrazone (FCCP), 0.5 µM antimycin A, and 0.5µM rotenone.

CRISPR/Cas9 knockout: Guide RNAs (gRNAs) targeting ALDH2 were designed using the Benchling CRISPR tool (https://www.benchling.com/crispr), selecting sequences predicted to minimize off-target effects. The selected gRNA was designed against Exon 2 of the reference ALDH2 transcript ENST00000261733.7 (ALDH2-201), on the negative strand (−1), with the sequence 5′-CCAGTGGACGGATTGACGGT-3′ and PAM sequence GGG. The ribonucleoprotein (RNP) was complexed at Cas9:sgRNA ratio 1:1.2 as previously described [47]. Briefly, 92.5pmol of Alt-R® S. pyogenes HiFi Cas9 protein (IDT #1081061) with 111pmol of Alt-R® CRISPR-Cas9 sgRNA were incubated at 25°C for 10 minutes.
0.5×10^6 H1975 Osi-R cells were harvested, washed three times with PBS without Ca2+ and Mg2+, and resuspended in 100 µL of Buffer R (Invitrogen #A56773). To determine optimal nucleofection conditions, cells were first electroporated with a GFP plasmid under three different programs using the Neon Transfection System (Thermo Fisher Scientific): 1200 V, 20 ms pulse width, 4 pulses; 1550 V, 10 ms pulse width, 3 pulses; and 1450 V, 10 ms pulse width, 4 pulses. Transfection efficiency was assessed by flow cytometry based on GFP fluorescence, to identify a program allowing efficient delivery while preserving cell viability. The 1450 V, 10 ms, 4 pulses program was selected for subsequent experiments based on its high transfection efficiency combined with high cell viability. For the gene editing experiment, the cell suspension in Buffer R was then combined with RNP complex and electroporated using this selected program with Neon 100 µL tips (Invitrogen #MPK10025). Immediately after nucleofection, cells were transferred to 6-well plates in antibiotic-free complete medium. The culture medium was replaced the following day with complete culture medium containing antibiotics. Once cells reached confluence, knockout efficiency was assessed by a T7 Endonuclease I (T7EI) assay according to the manufacturer's protocol (New England Biolabs # M0302S). Upon confirmation of successful editing, cells were seeded at single-cell density with the Cell Sorter CytoFLEX SRT instrument (Beckman Coulter) in 96-well plates to generate clonal populations. Clones were expanded and subsequently subjected to Sanger sequencing to confirm target gene knockout.

Genotyping of the clones and Sanger sequencing: Genomic DNA was extracted from individual clones using the NZYTech Tissue gDNA Isolation Kit (NZYTech #MB13502) according to the manufacturer's protocol. The genomic region flanking the CRISPR editing site for ALDHA2 was amplified by PCR using NZYTaq II enzyme (NZYTech #MB36401) and the following primers: forward 5′-CCTGTGCTTTTCATTTGTAGGCT-3′ and reverse 5′-CAGTTTCGATTGGTTCCTACAGT-3′, generating a 603 bp amplicon. PCR amplification was performed under the following cycling conditions: initial denaturation at 95°C for 2 min, followed by 35 cycles of 95°C for 40 s, 59°C for 30 s, and 72°C for 30 s, with a final extension at 72°C for 10 min. PCR products were resolved on a 1% agarose gel stained with SYBR Safe DNA Gel Stain (Invitrogen #S33102) to confirm successful amplification. PCR products were subsequently purified using the DNA Clean & Concentrator-5 kit (Zymo Research #D4003) and sent for Sanger sequencing. The resulting sequences were aligned to the reference genomic sequence using the Benchling alignment tool (https://www.benchling.com/alignments) to identify knockout alleles and other editing events at the target locus. Editing efficiency and indel composition were further analyzed using the Inference of CRISPR Edits (ICE) tool (https://ice.editco.bio/#/).

IC50 assay: Cell viability was assessed using the Trypan Blue exclusion assay, and IC50 values were calculated based on the number of viable cells relative to DMSO-treated controls using an automated cell counter (Countess, Life Technologies). Osimertinib IC50 values were determined following treatment with increasing concentrations of osimertinib (0-4 μM) for 72 h in Par cells, as well as in the OsiR CRISPR-Cas9-derived WT control clone and Aldh2 homozygous knockout (KO) clone. In parallel, H1975 OsiR cells were co-treated with Disulfiram (35 nM; (MedChemExpress, #HY-B0240) and increasing concentrations of osimertinib (0-4 μM), and IC50 values were determined after 72 h of drug exposure. Data are presented as the mean of three independent experiments.

Cell culture medium collection for exometabolome profiling: H1975P, OsiR, OsiR WT, and OsiR Aldh2 KO cells were cultured as biological replicates (n=3) per condition, unless otherwise stated, for 72 hours at 37°C in a humidified incubator with 5% CO_2, until reaching 90-100% confluence. The cell culture medium containing the exometabolome was then collected for further processing. Cells were detached and counted using a hemocytometer to enable normalization of metabolite levels.

Pyruvate Quantification by UHPLC-HRMS: Pyruvate levels were quantified by LC-HRMS. Analyses were carried out on an ultra-High-Performance Liquid Chromatography system (UHPLC; Vanquish Flex Binary pump) coupled with a diode array detector (DAD) and a high resolution (HR) Q Exactive Plus MS, based on Orbitrap technology, equipped with a heated electrospray ionization (HESI) source (Thermo Fischer Scientific Inc., Bremem, Germany). Chromatographic separation was achieved on a Zorbax® Eclipse Plus Phenyl-Hexyl Column (4.6 x 250 mm, 5 μm; Agilent Technologies, CA, USA) with a flow rate of 0.8 mL/min and a 1:1 split between the HRMS and DAD/UV detectors. The injections volume was 2 μL, and the column temperature was maintained at 40°C. Eluents consisted of MeOH/HCOOH 0.5% v/v (solvent B) and H_2O/HCOOH 0.5% v/v (solvent A), both of ultra-purity grade (ROMIL Ltd, Cambridge, UK). The gradient was as follows: 0-15 min: isocratic 100% A; 15-25 min: linear gradient from 0 to 80% B; 25-35 min: linear gradient from 80% to 100% B; 35-37 min (2 minutes): isocratic 100% B.; 37-44 min: re-equilibration with 100% solvent A. HRMS parameters were as follows: ionization was performed in both positive and negative modes: nebulization voltage 3400 V (+) and 3200 V(-), capillary temperature 290°C, sheath gas (N_2) 24 (+) and 28 (-) arbitrary units, auxiliary gas (N_2) 5 (+) and 4 (-) arbitrary units, S lens RF level 50. Full scan mode was used over an m/z range of 54-800, with a resolution of 70,000 at m/z 200. Data acquisition and analysis were conducted using Xcalibur 3.1 software (Thermo Fischer Scientific Inc., Bremen, Germany). LCMS files were processed using Xcalibur Version 4.1.0.0. Extracted Ion Chromatograms (EIC) were obtained by exact mass ranges (calculated from molecular formula $C_nH_nO_nP_aN_nS_n$, -H for negative ions, +H for positive ions) with ± 3 ppm (ΔM/M) $*10^6$ accuracy. Chromatogram peaks were manually integrated, and quantitative performed in Microsoft Excel.

Lactate Quantification by RP-HPLC-DAD: Due to its high extracellular concentration (mM), which saturates HRMS detectors, lactate was quantified by reversed-phase HPLC (RP-HPLC) with diode array detection (HPLC-DAD)[57]. For RP-HPLC-DAD analysis, samples were diluted 1:5 times in 5 mM sulfuric acid, filtered using 0.20 μm RC Mini-Uniprep filters (Agilent Technologies, Italy), and injected (V_{inj}= 5μL) into the same column employed for

LC-HRMS analysis. Metabolite identification was based on standard retention times and UV spectra, and quantification was performed via calibration curves generated from analytical standards, with manual peaks integration.

Acetate and Acetaldehyde Quantification by Headspace GC-MS: Acetate and acetaldehyde were quantified by head space gas chromatography-mass spectrometry (HS-GC-MS). Acetaldehyde was measured directly, while acetate required derivatization with trialkyloxonium salts, since LCMS is not accurate in the determination of low MW metabolites. For acetate analysis, 500 µL of sample or standard solution (0, 50, 100, 250, 400 µg/mL from Certified Standard), 50 µL of $^{2}H_3$ acetate at 1000 µg/mL (Internal Standard), and 100 µL of 5 M H_2SO_4 were added to 10 mL HS vials and sealed immediately. Standards and samples were prepared in triplicate. Calibration curves for quantification were prepared by plotting the areas at m/z 43 /area at m/z 46 ratio vs [acetate]/[acetate $^{2}H_3$] concentration ratio, using Agilent MassHunter Quantitative Analysis (v10.2). Measurements were performed using an Agilent 6850 GC system equipped with a 5975c single quadrupole MS detector and a GC 80 CTC PAL ALS autosampler. Separations were performed in J&W DB-WAX-UI capillary columns (30.0 m, 250.00 µm internal diameter, 0.50 µm film thickness) at constant flow of 1.0 mL/min (average velocity: 36 cm/s; incubation temperature 80 °C; incubation time 600 s; 1000 µL injection volume). The oven temperature program was: initial temperature 50 °C (hold 5 min), ramp up to 150°C at 10°C/min (hold 2 min); ramp to 240°C at 20°C/min (hold 8.5 min); total run time 30 min. Pulsed Splitless inlet mode; initial temperature 200 °C, pressure 45.4 kPa, pulse pressure 120 kPa, pulse time 0.10 min, purge flow 200.0 mL/min, purge time 0.10 min, total flow 203.7 mL/min, gas type helium; transfer line temperature 250 °C; SIM (Selected Ion Monitoring) mode: EI ionization mode at 70eV electron energy; Ion Source Temp. 250°C; Quadrupole Temperature: 150°C; SIM mode was used with acquisition at m/z 43, 46, 60, and 63 (Dwell Time 100 ms). Quantifier ions: 43 and 46; qualifier ions: 60 and 63. Data acquisition was managed via MSD ChemStation (Agilent, vE.02.02).

Exometabolomic profiling and acetate isotope-tracing: For exometabolomic and isotope-tracing analyses, H1975 Par and OsiR cells were cultured for 48 h in complete medium containing 2 g/L glucose, with 50% of the glucose replaced by uniformly labelled U-^{13}C-glucose. Following isotopic labelling, conditioned culture media were collected and processed for [U^{13}C]-acetate analysis. For metabolite extraction, 20 µL aliquots of conditioned medium were deproteinized with 300 µL of cold methanol followed by 20 minutes of centrifugation at 17000 x g at 4°C. Then, 20 µL of sodium hydroxide (1 N; Merck KGaA, Darmstadt, Germany) were added prior to sample drying. Samples were derivatized using N-(tert-butyldimethylsilyl)-N-methyltrifluoroacetamide (MTBSTFA; Merck KGaA, Darmstadt, Germany) for 1 h at 60°C. Acetate was quantified using [2H3]-acetate as an internal standard.
Samples were analyzed by gas chromatography coupled with single-quadrupole mass spectrometry (GC 7890A/MS 5975C, Agilent Technologies, Santa Clara, CA, USA) equipped with an HP-5Q capillary column (30 m × 0.25 mm i.d. × 0.25 µm film thickness; Agilent Technologies). The mass spectrometer operated in electron impact ionization mode (70 eV), and metabolites were analyzed in selected ion monitoring (SIM) mode. Isotopic enrichment was calculated as the tracer-to-tracee ratio (TTR), defined as the ratio between labelled ([M+n]) and unlabeled ([M+0]) isotopologues after correction for natural isotope abundance. For acetate, the monitored fragment was m/z 117 ([M−57]+), whereas labelled acetate was quantified using the isotopic fragment m/z 119 ([13C2]-acetate). The m/z 120 fragment ([2H3]-acetate) was used as the internal standard.

NADP/NADPH measurements: Intracellular $NADP^+$ and NADPH levels were measured using the NADP/NADPH Assay Kit (Abcam, #ab65349) according to the manufacturer's instructions. Briefly, H1975 OsiR CRISPR-Cas9-derived WT and Aldh2 KO cells were lysed, and the resulting lysates were further clarified using 10 kDa molecular weight cut-off spin columns (Merck Millipore, Amicon Ultra-0.5 Centrifugal Filter Unit, #UFC8010) in a swinging-bucket rotor (4,000 × g, 40 min, 4°C). Fifty µL of the clarified lysates were then used for $NADP^+$ and NADPH quantification. NADPH and total NADP (NADPt) levels were determined according to the manufacturer's protocol. Data were normalized to cell number and expressed as mean ± SD of biological replicates.

Structural Modeling: Structural models were based on the cryo-EM structure of the complete human ATP synthase complex (excluding DAPIT (Diabetes-Associated Protein in Insulin-sensitive Tissue) subunit; PDB ID: 8H9T [48, 49]), which detaches during purification but does not impair ATP synthase function. Missing residues were

reconstructed using the Swiss-Model web server, and the K45Q mutant was modelled using PyMol v.3.1 mutagenesis tool.

Protein Orientation and Membrane Embedding: The proper orientation of the proteins within the lipid bilayer was obtained from the Orientations of Proteins in Membranes (OPM) database [50] associated Mg^{2+} ions. Hydrogens were added using Chimera 1.18, optimizing H-bond networks and protonation states of histidine residues. OPM-aligned proteins were embedded in a homogeneous 200 x 200 Å (X, Y dimensions), composed of 1-palmitoyl-2-oleoyl-sn-*glycero*-3-phosphocholine (POPC) bilayer using the CHARMM-GUI web server [51].

Molecular Dynamics Simulations: MD simulations of protein-ATP/ADP-Mg^{2+}-membrane complexes were carried out with Amber v.24 [52]. CHARMM-GUI inputs were converted into Amber-compatible file formats using AmberTools scripts, specifically a modified version of charmmlipid2amber.py (charmmlipid2amber_python312.py) for Python 3.12 compatibility, and pdb4amber. Force fields included ff19SB for the protein [53], lipid21 for the membrane [54] and GAFF for small molecules [54]. $Mg2^{+}$ (ions234lm_1264_tip3p), and Na^{+}/Cl^{-} counterions were modelled using the monovalent and divalent parameters suitable for the TIP3P water molecule force field. Non-bonded interactions were computed with a 10 Å cutoff for both Coulomb and van der Waals potentials, while long-range electrostatic interactions were computed using the particle mesh Ewald method. Pressure was controlled via the Berendsen barostat, and temperature was maintained constant using the Langevin thermostat. Molecular dynamics simulations were performed in the NPT ensemble, where the number of particles (N), pressure (P), and temperature (T) are kept constant. This ensemble allows the system to adjust its volume naturally to maintain a realistic pressure, which is particularly important for membrane-embedded proteins. The minimization and equilibration protocol was adapted from a recent Github procedure optimized for in-membrane simulations[54] (https://github.com/callumjd/AMBER-Membrane_protein_tutorial/blob/master/README.md). Briefly, initial minimization consisted of 500 steps of the steepest descent algorithm, followed by 500 steps of the conjugate gradient algorithm, then an extensive minimization of 5000 steps of steepest descent plus 5000 steps of conjugate gradient. The first production run (0.42 ns) involved heating the system up to 100 K with positional restraints on protein, ligands, and membrane. Subsequently, a second heating step (0.6 ns) was performed to bring the system to 298 K, while maintaining the same restraints. This was followed by a 1 ns NPT equilibration with restraints on the receptor backbone and ligands, and an additional 1 ns production run under NPT conditions with restraints only on protein Cα and ligands. A final 5 ns equilibration without restraints was performed, followed by a 100 ns production run in the NPT ensemble.

Trajectory Analysis: MD trajectories were analyzed using CPPTRAJ to determine RMSD, perform clustering and PCA. Cluster analysis was carried out using the average-linkage algorithm with ten clusters. Dynamic cross-correlation maps (DCCM) and Normal Mode Analysis were performed using the Bio3d R package[31]. Interactions were analyzed using the getcontact Python library (https://getcontacts.github.io/). Figures were generated with PyMol v.3.1, except DCCM matrices and RMSD plots, which were produced using matplotlib-based Python scripts.

Transgenic mice and Drug Treatments: Generation of bi-transgenic mice carrying the *CCSP-rtTA* and TetO-regulated *EGFR* $^{L858R/T790M}$ transgenes, and genotyping, was performed as previously described [2, 55]. The expression of mutant EGFR and the development of lung tumors were induced by feeding 8- to 10-week-old mice with doxycycline impregnated food pellets (0.200 g/kg Rodent diet PF4184, Mucedola). Control mice were either $CCSP^{-}$/$EGFR^{+}$ or $CCSP^{+}$/$EGFR^{-}$, also treated with doxycycline. Mice were treated with osimertinib (10 mg/kg in 1% DMSO and 30% PEG in H_2O, oral gavage twice per week), or with vehicle control (1% DMSO and 30% PEG in H_2O). All m ice were housed in a sterile-barrier facility, and all experiments were approved by the Italian Ministry of Health (488/2022-PR).

Mouse lung and tumor dissociation into single cells: Mouse pulmonary tissue (healthy and tumor) was dissociated for downstream single-cell RNA sequencing using the Tumor Dissociation Kit (Miltenyi Biotec, #130-096-730). Briefly, tissue was placed in a petri dish on ice and cut into small pieces of 2-4 mm. The pieces were then infused with RPMI/enzyme mix (Miltenyi Biotec kit), transferred to a gentleMACS C tube containing RPMI/enzyme mix, attached to the sleeve of the Miltenyi Biotec gentleMACS Octo Dissociator, and run using the "37C_m_TDK_2" program. After completion of the program, cells were spun down at 300 x g for 10 min at 4°C, resuspended in RPMI-2% FBS,

and passed through a 70 μm strainer. The centrifugation step was then repeated. The resulting cell pellet was treated with 1 ml of ACK solution for 7 min at RT, and lysis stopped with 4 ml of RPMI 0.2% FBS. After centrifugation, cells were suspended in 1 ml RPMI-2% FBS and passed through a 70 μm cell strainer to obtain a single-cell suspension, as previously reported [56, 57].

scRNA-sequencing analysis: Murine lung tumor cells from $EGFR^{LT}$ mice treated with vehicle (Vehicle, n = 4), short-term osimertinib (OsiS, n= 4), or long-term osimertinib (OsiR, n = 6), for a total of 14 samples, were processed using the Chromium Next GEM Single Cell 3' Reagent Kit v2 (10x Genomics). scRNA-seq libraries were prepared and sequenced on the Illumina NovaSeq6000 platform following the standard protocol. Sequenced scRNA-seq libraries were demultiplexed and processed using the CellRanger Single-Cell Software Suite (v.7.1.0, 10x Genomics). The mouse genome GRCm38 was used as reference for the read alignment step. Unique molecular identifiers (UMIs) were quantified to generate a cell-by-gene count matrix for each sample. These matrices were then imported into the R environment (v.4.1.3) and analyzed using Seurat v.5.2.1 [58]. Specifically, cells expressing <200 genes or >8,000 genes were excluded, because a low gene count suggests false positives or low viability, whereas a high count indicates potential doublets. In addition, cells with >20% of transcripts originating from mitochondrial (mt) genes were removed, because they probably represent stressed or dying cells. Unique molecular identifier (UMI) counts were log-normalized and scaled by a factor of 10,000. The top 20% most variable genes were selected for further analysis. Cell-cycle scores were assigned using the Cell-Cycle Scoring function with reference gene lists. Data were scaled, and sources of variability were regressed out by including the UMI count, mitochondrial gene percentage, and cell-cycle difference as variables in the vars.to.regress argument. Cell-cycle difference was defined as the difference between the S phase and G2/M phase module scores. Downstream analysis was conducted on all 50 components computed using PCA. To mitigate sample-related variability and 10x chemistry version bias, data integration was performed using the Harmony package (v.1.0) [59]. Uniform manifold approximation and projection (UMAP) dimensionality reduction and the cell neighbor graph were computed with default parameters using the first 30 of 50 Harmony PCs [60]. Clusters were identified with the original Louvain algorithm through the FindClusters function at various resolutions, and cluster markers were determined using the FindAllMarkers function in Seurat. For the downstream analyses, only clusters computed at resolution r= 0.6 were considered. Each cluster was compared with all other cells using Wilcoxon's rank-sum test for significance. Genes expressed in >0% of cells in either group, with an adjusted p-value $P < 0.05$ and a $\log_2$(FoldChange) > 0.25, were considered to markers.

Epithelial AT2-like cluster analysis and gene signature scoring: Clusters identified at resolution 0.6 and annotated as epithelial were selected for downstream visualization analyses. To assess AT2-like features, normalized expression of *Sftpc* was visualized on the non-split UMAP embedding using the FeaturePlot function in Seurat. UMAP embeddings were generated and displayed either as a single panel or split by experimental condition (Vehicle, OsiS, and OsiR), maintaining consistent cluster color assignments across panels. For metabolic gene analysis, the expression of selected genes (*Ldha, Aldh2, Aldh7a1, Aldoa, Pdha1, Tkt*, and *Sdha, Sdhb, Sdhc, Sdhd*) was evaluated individually and as a combined gene signature. For signature-based analyses, normalized expression values were scaled across cells to obtain z-scores. The mean z-score for each gene set was calculated per condition and used to generate heatmaps representing relative expression patterns across Vehicle, OsiS, and OsiR samples. Heatmaps were generated in R using z-scored average expression values.

Data Availability: RNA sequencing, mitochondrial DNA sequencing and Whole genome sequencing data were deposited into EMBL-EBI's ArrayExpress under accession number E-MTAB-15298, E-MTAB-15301, E-MTAB-15299, respectively. scRNAseq data were deposited to GEO under accession number GSE320055.

FUNDING: This work was supported by the AIRC Investigator Grant 2021 (ID 25734), PNNR THE Spoke 1 Award, the PNRR-MCNT1-2023-12377671 Grant, the ELMO Pisa Foundation Grant, the FPS Grant 2024, and private donations from the Gheraldeschi and Pecoraro families to EL. AC was supported by the European Union - Next Generation EU, Mission 4 Component 2, project Strengthening BBMRL.it. AA acknowledges funding from A-0001263-00-00. Alessandra Giorgetti was supported by the Ministerio de Ciencia e Innovación, which is part of Agencia Estatal de Investigación (AEI), through the Retos Investigación Grant PID2022-140457OB-I00 funded by MCIU /AEI /10.13039/501100011033, grant no. AC23_2/00040 by ISCIII through AES 2023 and within the

European Joint Programme Rare Diseases framework, by Instituto de Salud Carlos III (ISCIII), and “Programa FORTALECE del Ministerio de Ciencia e Innovación” through the project number FORT23/00032. DRM was supported by the Scientific Foundation of the Spanish Association Against Cancer project number INVES2610039ROME. MMM was supported by the Government of Andorra with the predoctoral fellowship, ATC030-AND/2022. Amelia Gastaldelli received funding from the European Union's Horizon Europe Research and Innovation Programme for the project PAS GRAS: De-risking Metabolic, Environmental and Behavioral Determinants of Obesity in Children, Adolescents and Young Adults (Grant Agreement No. 101080329).

Authors’ contributions

GM designed the study, performed the experiments, analyzed and interpreted the data, drafted the manuscript, and critically revised the manuscript.

ECSM, Alessandra Gatta, FC, MMM and LM performed the experiments

RM, MM and AA performed the experiments and contributed to data analysis.

MDN, AC, LC, RA, NS, BC, MO, PP, GB, DRM and EM contributed to data analysis.

IM, AO, PD, Amalia Gastaldelli, and Alessandra Giorgetti contributed to data analysis and provided senior supervision for the analytical work.

GC contributed to data interpretation.

EB conceived and designed the study, interpreted the data, drafted the manuscript, and critically revised the manuscript.

EL conceived and designed the study, analyzed and interpreted the data, drafted the manuscript, and critically revised the manuscript.

All authors read and approved the final manuscript.

Ethics, Consent to Participate, and Consent to Publish: Not Applicable

The authors declare that they have no competing interests.

REFERENCES

1. Levantini E, Maroni G, Del Re M, Tenen DG: **EGFR signaling pathway as therapeutic target in human cancers.** *Semin Cancer Biol* 2022.
2. Ali A, Levantini E, Teo JT, Goggi J, Clohessy JG, Wu CS, Chen L, Yang H, Krishnan I, Kocher O, et al: **Fatty acid synthase mediates EGFR palmitoylation in EGFR mutated non-small cell lung cancer.** *EMBO Mol Med* 2018, **10**.
3. Ali A, Levantini E, Fhu CW, Teo JT, Clohessy JG, Goggi JL, Wu CS, Chen L, Chin TM, Tenen DG: **CAV1 - GLUT3 signaling is important for cellular energy and can be targeted by Atorvastatin in Non-Small Cell Lung Cancer.** *Theranostics* 2019, **9:**6157-6174.
4. Warburg O: **On the origin of cancer cells.** *Science* 1956, **123:**309-314.
5. Diaz-Ruiz R, Rigoulet M, Devin A: **The Warburg and Crabtree effects: On the origin of cancer cell energy metabolism and of yeast glucose repression.** *Biochimica et Biophysica Acta (BBA) - Bioenergetics* 2011, **1807:**568-576.
6. Ferreira LM: **Cancer metabolism: the Warburg effect today.** *Exp Mol Pathol* 2010, **89:**372-380.
7. Medes G, Paden G, Weinhouse S: **Metabolism of neoplastic tissues. XI. Absorption and oxidation of dietary fatty acids by implanted tumors.** *Cancer Res* 1957, **17:**127-133.
8. Schug ZT, Vande Voorde J, Gottlieb E: **The metabolic fate of acetate in cancer.** *Nat Rev Cancer* 2016, **16:**708-717.
9. Robey RB, Hay N: **Mitochondrial hexokinases, novel mediators of the antiapoptotic effects of growth factors and Akt.** *Oncogene* 2006, **25:**4683-4696.
10. Liberti MV, Locasale JW: **The Warburg Effect: How Does it Benefit Cancer Cells?** *Trends in Biochemical Sciences* 2016, **41:**211-218.
11. Colombaioni L, Onor M, Benedetti E, Bramanti E: **Thallium stimulates ethanol production in immortalized hippocampal neurons.** *PLoS One* 2017, **12:**e0188351.
12. Bramanti E, Onor M, Colombaioni L: **Neurotoxicity Induced by Low Thallium Doses in Living Hippocampal Neurons: Evidence of Early Onset Mitochondrial Dysfunction and Correlation with Ethanol Production.** *ACS Chem Neurosci* 2019, **10:**451-459.
13. Campanella B, Colombaioni L, Nieri R, Benedetti E, Onor M, Bramanti E: **Unraveling the Extracellular Metabolism of Immortalized Hippocampal Neurons Under Normal Growth Conditions.** *Front Chem* 2021, **9:**621548.
14. Colombaioni L, Campanella B, Nieri R, Onor M, Benedetti E, Bramanti E: **Time-dependent influence of high glucose environment on the metabolism of neuronal immortalized cells.** *Anal Biochem* 2022, **645:**114607.
15. Armanetti P, Cabrera San Millan E, Di Nardo M, Mercatelli R, Cavallini C, Crucitta S, Del Re M, Chiodi A, Mosca E, Consiglio A, et al: **Dual actionability of BMI1 activation and mitotic vulnerability defines adaptive Osimertinib resistance in EGFR-mutant NSCLC.** *Cell Death Dis* 2026.
16. Wu J, Chen Y, Lin Y, Lan F, Cui Z: **Cancer-testis antigen lactate dehydrogenase C4 as a novel biomarker of male infertility and cancer.** *Front Oncol* 2022, **12:**936767.
17. Peng W, Chen J, Xiao Y, Su G, Chen Y, Cui Z: **Cancer-Testis Antigen LDH-C4 in Tissue, Serum, and Serum-Derived Exosomes Serves as a Promising Biomarker in Lung Adenocarcinoma.** *Front Oncol* 2022, **12:**912624.
18. Muzio G, Maggiora M, Paiuzzi E, Oraldi M, Canuto RA: **Aldehyde dehydrogenases and cell proliferation.** *Free Radic Biol Med* 2012, **52:**735-746.
19. Dinavahi SS, Bazewicz CG, Gowda R, Robertson GP: **Aldehyde Dehydrogenase Inhibitors for Cancer Therapeutics.** *Trends Pharmacol Sci* 2019, **40:**774-789.
20. Sun X, Yegambaram M, Lu Q, Garcia Flores AE, Pokharel MD, Soto J, Aggarwal S, Wang T, Fineman JR, Black SM: **Mitochondrial fission produces a Warburg effect via the oxidative inhibition of prolyl hydroxylase domain-2.** *Redox Biol* 2025, **81:**103529.
21. Chen W, Zhao H, Li Y: **Mitochondrial dynamics in health and disease: mechanisms and potential targets.** *Signal Transduct Target Ther* 2023, **8:**333.

22. Ghosh D, Pakhira S, Ghosh DD, Roychoudhury S, Roy SS: **Ets1 facilitates EMT/invasion through Drp1-mediated mitochondrial fragmentation in ovarian cancer.** *iScience* 2023, **26:**107537.
23. Cao K, Riley JS, Heilig R, Montes-Gomez AE, Vringer E, Berthenet K, Cloix C, Elmasry Y, Spiller DG, Ichim G, et al: **Mitochondrial dynamics regulate genome stability via control of caspase-dependent DNA damage.** *Dev Cell* 2022, **57:**1211-1225 e1216.
24. Sabouny R, Shutt TE: **The role of mitochondrial dynamics in mtDNA maintenance.** *J Cell Sci* 2021, **134**.
25. Dua N, Seshadri A, Badrinarayanan A: **DarT-mediated mtDNA damage induces dynamic reorganization and selective segregation of mitochondria.** *J Cell Biol* 2022, **221**.
26. Schagger H, Link TA, Engel WD, von Jagow G: **Isolation of the eleven protein subunits of the bc1 complex from beef heart.** *Methods Enzymol* 1986, **126:**224-237.
27. Perez-Perez R, Lobo-Jarne T, Milenkovic D, Mourier A, Bratic A, Garcia-Bartolome A, Fernandez-Vizarra E, Cadenas S, Delmiro A, Garcia-Consuegra I, et al: **COX7A2L Is a Mitochondrial Complex III Binding Protein that Stabilizes the III2+IV Supercomplex without Affecting Respirasome Formation.** *Cell Rep* 2016, **16:**2387-2398.
28. Lu L, Chen L, Gao F, Xu C, Ni C, Qian W: **Rab5if is a potential therapeutic target of NSCLC.** *Cancer Genet* 2025, **294-295:**123-135.
29. He J, Ford HC, Carroll J, Douglas C, Gonzales E, Ding S, Fearnley IM, Walker JE: **Assembly of the membrane domain of ATP synthase in human mitochondria.** *Proc Natl Acad Sci U S A* 2018, **115:**2988-2993.
30. Lai Y, Zhang Y, Zhou S, Xu J, Du Z, Feng Z, Yu L, Zhao Z, Wang W, Tang Y, et al: **Structure of the human ATP synthase.** *Mol Cell* 2023, **83:**2137-2147.e2134.
31. Durand PT, G; Sanejouand, YH: **A new approach for determining low-frequency normal modes in macromolecules.** *Biopolymers* 1994, **34:**759-771.
32. Bauer JA, Bauerová-Hlinková V: **Normal Mode Analysis: A Tool for Better Understanding Protein Flexibility and Dynamics with Application to Homology Models.** In *Homology Molecular Modeling - Perspectives and Applications.* Edited by Maia RT, Maciel de Moraes Filho R, Campos MDA. Rijeka: IntechOpen; 2020
33. Li G, Cui Q: **Analysis of Functional Motions in Brownian Molecular Machines with an Efficient Block Normal Mode Approach: Myosin-II and Ca²⁺-ATPase.** *Biophysical Journal* 2004, **86:**743-763.
34. Dobin A, Davis CA, Schlesinger F, Drenkow J, Zaleski C, Jha S, Batut P, Chaisson M, Gingeras TR: **STAR: ultrafast universal RNA-seq aligner.** *Bioinformatics* 2013, **29:**15-21.
35. Liao Y, Smyth GK, Shi W: **featureCounts: an efficient general purpose program for assigning sequence reads to genomic features.** *Bioinformatics* 2014, **30:**923-930.
36. Robinson MD, Oshlack A: **A scaling normalization method for differential expression analysis of RNA-seq data.** *Genome Biol* 2010, **11:**R25.
37. Chen Y, Chen L, Lun ATL, Baldoni PL, Smyth GK: **edgeR v4: powerful differential analysis of sequencing data with expanded functionality and improved support for small counts and larger datasets.** *Nucleic Acids Res* 2025, **53**.
38. Ritchie ME, Phipson B, Wu D, Hu Y, Law CW, Shi W, Smyth GK: **limma powers differential expression analyses for RNA-sequencing and microarray studies.** *Nucleic Acids Res* 2015, **43:**e47.
39. Kuleshov MV, Jones MR, Rouillard AD, Fernandez NF, Duan Q, Wang Z, Koplev S, Jenkins SL, Jagodnik KM, Lachmann A, et al: **Enrichr: a comprehensive gene set enrichment analysis web server 2016 update.** *Nucleic Acids Res* 2016, **44:**W90-97.
40. Chen EY, Tan CM, Kou Y, Duan Q, Wang Z, Meirelles GV, Clark NR, Ma'ayan A: **Enrichr: interactive and collaborative HTML5 gene list enrichment analysis tool.** *BMC Bioinformatics* 2013, **14:**128.
41. Xie Z, Bailey A, Kuleshov MV, Clarke DJB, Evangelista JE, Jenkins SL, Lachmann A, Wojciechowicz ML, Kropiwnicki E, Jagodnik KM, et al: **Gene Set Knowledge Discovery with Enrichr.** *Curr Protoc* 2021, **1:**e90.

42. Chaudhry A, Shi R, Luciani DS: **A pipeline for multidimensional confocal analysis of mitochondrial morphology, function, and dynamics in pancreatic beta-cells.** *Am J Physiol Endocrinol Metab* 2020, **318:**E87-E101.
43. Li H: **New strategies to improve minimap2 alignment accuracy.** *Bioinformatics* 2021, **37:**4572-4574.
44. Weissensteiner H, Forer L, Fendt L, Kheirkhah A, Salas A, Kronenberg F, Schoenherr S: **Contamination detection in sequencing studies using the mitochondrial phylogeny.** *Genome Res* 2021, **31:**309-316.
45. Rath S, Sharma R, Gupta R, Ast T, Chan C, Durham TJ, Goodman RP, Grabarek Z, Haas ME, Hung WHW, et al: **MitoCarta3.0: an updated mitochondrial proteome now with sub-organelle localization and pathway annotations.** *Nucleic Acids Res* 2021, **49:**D1541-D1547.
46. Auwera GAVd, O'Connor BD: **Genomics in the Cloud : Using Docker, GATK, and WDL in Terra.** Sebastopol: O'Reilly Media, Incorporated; 2020.
47. Romero-Moya D, Torralba-Sales E, Calvo C, Marin-Bejar O, Magallon-Mosella M, Distefano M, Pera J, Castano J, De Giorgio F, Gonzalez J, et al: **CRISPR-engineered human GATA2 deficiency model uncovers mitotic dysfunction and premature aging in HSPCs, impairing hematopoietic fitness.** *Leukemia* 2025, **39:**3015-3025.
48. Carroll J, He J, Ding S, Fearnley IM, Walker JE: **Persistence of the permeability transition pore in human mitochondria devoid of an assembled ATP synthase.** *Proc Natl Acad Sci U S A* 2019, **116:**12816-12821.
49. Lai Y, Zhang Y, Zhou S, Xu J, Du Z, Feng Z, Yu L, Zhao Z, Wang W, Tang Y, et al: **Structure of the human ATP synthase.** *Mol Cell* 2023, **83:**2137-2147 e2134.
50. Lomize MA, Pogozheva ID, Joo H, Mosberg HI, Lomize AL: **OPM database and PPM web server: resources for positioning of proteins in membranes.** *Nucleic Acids Res* 2012, **40:**D370-376.
51. Jo S, Kim T, Iyer VG, Im W: **CHARMM-GUI: a web-based graphical user interface for CHARMM.** *J Comput Chem* 2008, **29:**1859-1865.
52. Case DA, Aktulga HM, Belfon K, Cerutti DS, Cisneros GA, Cruzeiro VWD, Forouzesh N, Giese TJ, Gotz AW, Gohlke H, et al: **AmberTools.** *J Chem Inf Model* 2023, **63:**6183-6191.
53. Tian C, Kasavajhala K, Belfon KAA, Raguette L, Huang H, Migues AN, Bickel J, Wang Y, Pincay J, Wu Q, Simmerling C: **ff19SB: Amino-Acid-Specific Protein Backbone Parameters Trained against Quantum Mechanics Energy Surfaces in Solution.** *J Chem Theory Comput* 2020, **16:**528-552.
54. Dickson CJ, Walker RC, Gould IR: **Lipid21: Complex Lipid Membrane Simulations with AMBER.** *J Chem Theory Comput* 2022, **18:**1726-1736.
55. Regales L, Balak MN, Gong Y, Politi K, Sawai A, Le C, Koutcher JA, Solit DB, Rosen N, Zakowski MF, Pao W: **Development of new mouse lung tumor models expressing EGFR T790M mutants associated with clinical resistance to kinase inhibitors.** *PLoS One* 2007, **2:**e810.
56. Maroni G, Bassal MA, Krishnan I, Fhu CW, Savova V, Zilionis R, Maymi VA, Pandell N, Csizmadia E, Zhang J, et al: **Identification of a targetable KRAS-mutant epithelial population in non-small cell lung cancer.** *Commun Biol* 2021, **4:**370.
57. Zilionis R, Nainys J, Veres A, Savova V, Zemmour D, Klein AM, Mazutis L: **Single-cell barcoding and sequencing using droplet microfluidics.** *Nat Protoc* 2017, **12:**44-73.
58. Stuart T, Butler A, Hoffman P, Hafemeister C, Papalexi E, Mauck WM, 3rd, Hao Y, Stoeckius M, Smibert P, Satija R: **Comprehensive Integration of Single-Cell Data.** *Cell* 2019, **177:**1888-1902 e1821.
59. Korsunsky I, Millard N, Fan J, Slowikowski K, Zhang F, Wei K, Baglaenko Y, Brenner M, Loh PR, Raychaudhuri S: **Fast, sensitive and accurate integration of single-cell data with Harmony.** *Nat Methods* 2019, **16:**1289-1296.
60. McInnes L HJ, Saul N, Großberger L.: **UMAP: Uniform Manifold Approximation and Projection.** *J Open Source Softw* 2018.